CZECH TECHNICAL UNIVERSITY IN
PRAGUE

Faculty of Nuclear Sciences and Physical
Engineering

Department of Physics

Research project

Properties of the diboson production in the ATLAS experiment at the LHC

Bc. Kateřina Moudrá

Supervisor: Mgr. Oldřich Kepka, Ph.D.

Prague, 2014

Prohlášení:

Prohlašuji, že jsem svou práci vypracovala samostatně a použila jsem pouze podklady (literaturu, software, atd.) uvedené v přiloženém seznamu.

Nemám závažný důvod proti užití tohoto školního díla ve smyslu 60 Zákona 121/2000 Sb., o právu autorském, o právech souvisejících s právem autorským a o změně některých zákonů (autorský zákon).

V Praze dne

Acknowledgement

Abstract

Studying diboson production processes provides opportunity to test the electroweak sector of the Standard Model. The charged triple and quartic gauge boson coupling lagrangian contains parameters, which have fixed values in the SM. Deviations of the coupling parameters with respect to SM predictions could result from a new physics, e.g. from presence of new particles. Diboson production plays also important role as a background in rare processes with large missing energy (e.g. H→WW, SUSY searches...).

In this work, the existing measurement of WW production cross section by the ATLAS experiment at the LHC at $\sqrt{s} = 7$ TeV with integrated luminosity of 4.6 fb^{-1} was reproduced at the particle level. This measurement and also existing ZZ measurement were implemented to the Rivet framework, which enables direct comparison of the measurements with any theoretical prediction (new models, studies of theoretical uncertaininies such as dependence on parton distribution functions, renormalisation and factorisation scales etc.).

Contents

List of Figures

List of Tables

Chapter 1

Standard Model and the LHC

The main topic of this thesis is the diboson production with W and Z bosons decaying leptonically. In this Chapter, the basic theoretical framework for the production calculations will be described. Then, the experimental apparatus, LHC, together with the ATLAS experiment will be shortly presented.

1.1   Standard Model

Standard Model [1] is a theory summarising knowledge about known particles and their interactions. It is a quantum field theory. Emerging as excitations of a specific field, there are three main classes of fundamental particles in the Standard Model:

- Leptons (e, μ, τ, ν_e, ν_μ, ν_τ) and quarks (u, d, c, s, t, b) that are fermions and constituents of matter.

- Gauge vector bosons (g, γ, W, Z) that mediate interactions.

- Scalar Higgs boson, H, that gives mass to fundamental particles.

The fundamental particles and their main characteristics, such as mass, charge and spin, are summarized in Figure 1.1. Being building blocks of the hadronic matter, the quarks bind together in multiplets to form baryons and mesons. Both quarks and leptons are observed in three generations (e.g. $e\nu_e$,ud, cs), which differ in quantum numbers and mass. They are identified by weak interaction, which only allows transition of pair of particles from one generation to another.

Each of the fundamental interactions in the Standard Model is described by the specific gauge theory with a symmetry group. These interactions are: strong (with SU(3) symmetry group), electromagnetic (with U(1) symmetry group) and weak (with SU(2) symmetry group). The principle of an interaction can be explained in terms of an exchange of a specific force mediator, gauge boson. The electromagnetic interaction is described by an exchange of a massles photon, γ, which couples to electric charge. The strong interaction is mediated by 8 massles gluons, which carry color charge. The weak interaction is described by exchange of the massive W^+, W^- and Z bosons. Connecting the three interactions, Standard Model represents a non-Abelian gauge theory with a U(1)×SU(2)×SU(3) group. There is one more fundamental interaction, the gravitation, which is not embedded in the Standard Model. The mediator of this interaction has not been observed yet. The list of interactions, their mediators and approximate range is given in Table 1.1.

The diboson production disscussed in this thesis is closely related to the concept of the electroweak interaction, which unites the electromagnetic and the weak interaction
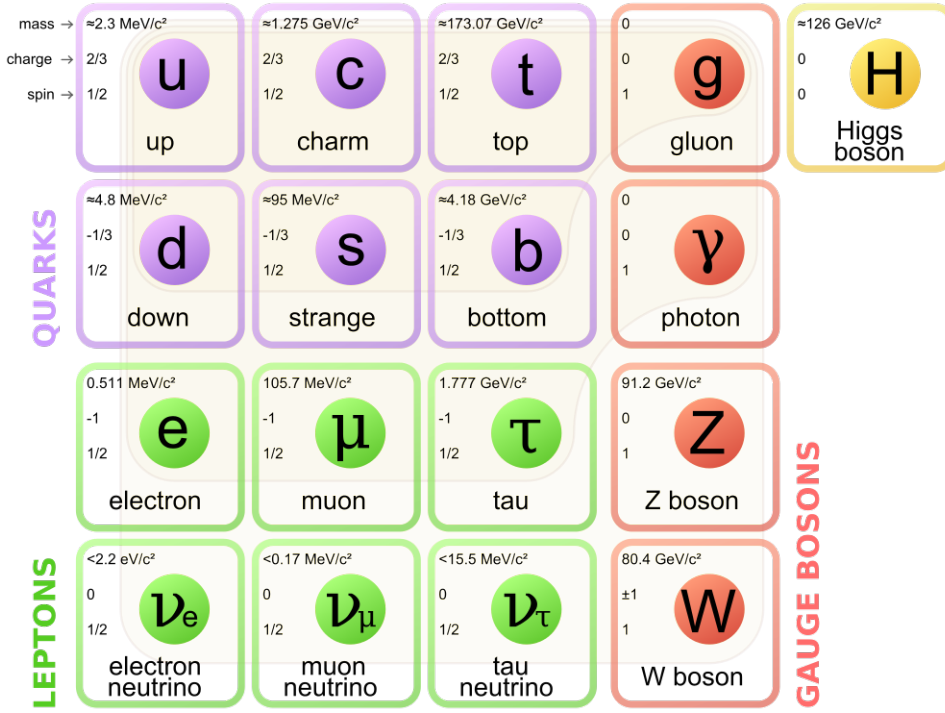
Figure 1.1: Summary of main properties (mass, charge and spin) of fundamental particles in the Standard Model, assuming three generations of quarks and leptons, gauge bosons and the Higgs boson [2].

Interaction	Gauge boson	Range	Relative force
Electromagnetic	Photon γ	∞	10^{-2}
Weak	Intermediate bosons W^{+-}, Z	10^{-18} m	10^{-7}
Strong	Gluon g	10^{-15} m	1
Gravitational	Graviton G (not observed yet)	∞	10^{-39}

Table 1.1: An overview of four fundamental interactions, their gauge bosons, range and relative force with respect to the strong interaction [1]. The first three interactions are described by the Standard Model.

into one theoretical framework. The significant difference of masses of electroweak gauge bosons (γ,W$^\pm$,Z) is caused by phenomena referred to as spontaneous symmetry breaking. The broken symmetry is a gauge symmetry (O(4)$\rightarrow$U(1)$\times$SU(2)), where gauge bosons have to be massless (no mass terms in the lagrangian.) The breaking itself is realized by the Higgs mechanism, in which the particles gain mass by interacting with a scalar Higgs field.

The next interaction assumed in the Standard Model is the strong interaction, which, by affecting quarks and gluons (carying colour charge), is responsible for the existence of all hadronic matter (protons, atomic nuclei etc). The gauge theory describing this interaction is referred to as Quantum Chromodynamics (QCD) and has interesting scale dependent behaviour, which can be described in terms of running coupling constant, α_s (or α_{QCD}). This variable dictates the strength of the strong interaction. Its dependence on the momentum scale, Q^2, is illustrated in Figure 1.2 and leads to the following two characteristics of the strong interaction:
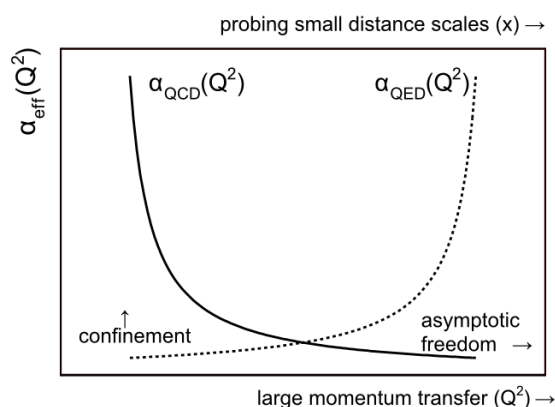
Figure 1.2: Runnning coupling constants $\alpha_{QCD}(Q^2)$ of the strong interaction and $\alpha_{QED}(Q^2)$ of the electromagnetic interaction and their dependence on the momentum scale Q^2 [3].

- Quark confinement - at long distances or low momentum transfers Q^2, i.e. as in "ordinary" hadronic matter, value of α_s is high. Quarks are strongly bound and confined in hadrons. This implies, that it is impossible to separate single free quark from a proton.

- Assymptotic freedom - at short distances and high energy scales, α_s assymptotically decreases. This behaviour is of high importance in high energy collission experiments, where partons in the protons behave almost as free particles and the small value of α_s allows perturbative calculations.

The value of strong coupling constant for the Z mass scale is $\alpha_s(m_Z) = 0.012$ [4]. In the gauge theory for electromagnetic interactions, Quantum Electrodynamics (QED), the running of coupling constant is exactly opposite. At low scales it goes to known value $\alpha_{QED} = \frac{1}{137} = 0.007$ [5]. The difference between running of QED and QCD coupling constants is due to different gauge structure allowing gluons interact with themselves in QCD.

The interactions of particles can be schematically depicted by Feynman diagrams. The construction of such diagrams is given by specific rules, which are determined by expandig

the evolution operator in the coupling constant. Since $\alpha_s(Q^2)$ is small for large Q^2, the assymptotic freedom allows this expansion. The diagrams of a certain process with the lowest order in $\alpha_s(Q^2)$ are referred to as the leading order (LO) diagrams. Diagrams with higher order in $\alpha_s(Q^2)$ are called next-to-leading order (NLO) diagrams. An example of LO and NLO Feynman diagrams for the $q{\rightarrow}qg$ process illustrates the Fig.1.3.
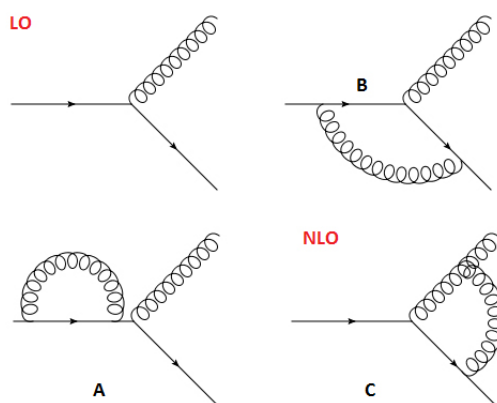
Figure 1.3: An example of LO and NLO Feynman diagrams for the q→qg process [6].

1.2 LHC

In the modern experimental particle physics, Standard Model processes are studied and tested in high energy particle collisions. Large Hadron Collider [7] (LHC) is a superconducting hadron accelerator and collider installed in a 27 km circumference tunnel, 45-170 m underground. It is located at CERN, at the France-Switzerland border close to Geneva.

LHC consists of two rings, each to be filled by one proton (or ion) beam. To make the protons collide, one ring is designed to circulate the beam clockwise and the other one to circulate the beam counter-clockwise. On the circuit, there are four interaction points, where the beams can meet. These interaction points correspond to the four main experiments at LHC: ATLAS, CMS, ALICE and LHCb.

The beam size can be described in terms of transverse emittance ϵ and amplitude function β. The transverse emittance ϵ is proportional to the size of the momentum phase space of the beam. The amplitude function β is determined by the configuration of focusing magnets and expresses the divergence of the beam. For the experiment, especially the value of β function at the interaction point, conventionally denoted as β^*, is important. Generally, the smaller is the β^*, the better focused beam we have.

The proton beam consists of separated proton bunches. At the LHC, under nominal operating conditions, there are 2808 bunches in one proton beam. Each bunch contains about 10^{11} protons. The bunches collide with a frequency of 40 MHz. During a collision, the bunches are few centimeters long and about 16 μm wide. The collisions are not precisely head-on but occur at a small angle of 150-200 μrad, in order to keep the interaction point in a small area.

Each bunch crossing produces many proton-proton (pp) interactions, referred to as *multiple proton-proton interactions* (in-time pile-up). One of the pp interactions typically produces significantly large amount of energy in the detector and one is ideally interested to study this interaction alone, which is not possible, due to the contamination of the event

by the other pp interactions. The mean number of interactions per bunch crossing for the recent runs was in the order of tens during 2012 and around 8 in 2011, depending on LHC setup as seen from Figure 1.4 (left).

For particle colliders, from the physical point of view, the most important performance parameters are the beam energy and the luminosity.

1.2.1 Beam energy

The cross section of processes important for this thesis increases with the beam energy. High energies allow to study the physics at higher transferred momentum scale, where the theory needs to be probed, because in this region the potentialy new processes might be seen. Being the last element of the accelerator complex, the LHC is designed to produce proton-proton collisions with a center-of-mass energy up to 14 TeV, which will be the highest center-of-mass energy ever reached in particle physics experiments.

The accelaration process [7] starts with dissociation hydrogen atoms using the electric field. The first machine in the chain, Linear Accelerator (LINAC), accelerates the protons to the energy of 50 MeV. Then, the beam is transferred to the Proton Synchrotron Booster (PBS), which accelerates the protons to 1.4 GeV. The process continues in the Proton Synchrotron (PS), where the beam gains energy of 25 GeV, followed by the Super Proton Synchrotron (SPS), to reach energy of 450 GeV. Then, the proton beam is injected to the LHC, where it is accelerated to the final energy.

The first data from proton-proton collisions at LHC were collected at reduced energies, 7 TeV in 2011 and 8 TeV in 2012. After the ongoing upgrade, in 2015, the center-of-mass energy is expected to reach 13 TeV.

1.2.2 Luminosity

The number of proton-proton collisions produced by the accelerator is proportional to luminosity. The higher the luminosity is, the better can be studied the rare processes. As a result, LHC is designed to produce events with high luminosities. The luminosity is defined as the proportionality factor between the number of events N, measured in the experiment, and the cross section of the event under study σ:

$$\mathcal{L} = \frac{N}{\sigma} = \frac{n_b N_b^2 f_{rev} \gamma}{4\pi \epsilon_n \beta^*} F,$$
(1.1)

where n_b is the number of bunches per beam, N_b the number of protons per bunch, f_{rev} the revolution frequency, $\epsilon_n = \frac{\epsilon}{\gamma}$ the normalized trasverse beam emmitance and β^* the amplitude function β at the collision point. F is a factor that takes into account, that due to collision angle of the two beams, the area of interaction is reduced. This definition of luminosity considers the immediate number of interaction per second.

One can see that more bunches in the LHC, more protons in a bunch (beam intensity) or smaller β^* (as a result of better beam focusing) lead to higher achieved $\mathcal{L}$.

During the run, as the bunches undergo collisions, the intensity of the proton beams decreases. As a result, the luminosity is not constant, but decreases. The integrated luminosity is used to describe number of events collected over the full running time of the machine. It is defined as the integral of the luminosity with respect to time:

$$L = \int \mathcal{L} dt.$$
(1.2)

The ATLAS recorded luminosity as a function of time in 2011 run is in Figure 1.4(left). In 2011 run, the total integrated luminosity was around 5 fb^{-1}, in 2012 run it was around 20 fb^{-1}
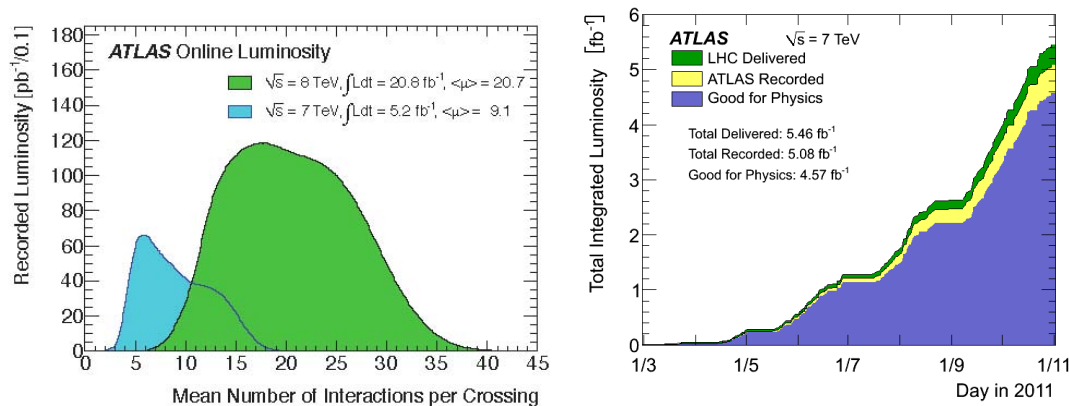

Figure 1.4: Left: Mean number of interactions per bunch-crossing. Right: ATLAS recorded luminosity as a function of time in 2011 physics run at 7 TeV [8].

1.3   Proton-proton collision

After the short overview of beam parameters, our discussion leads to the proton-proton collisions during the bunch-crossing. Although in diboson production we want to study electroweak sector of the Standard Model, the attention cannot be focused only on this part of the theory, because colliding protons are compound systems of strongly interacting objects. It is important to notice, that the colliding objects are not protons itself, but their inner components, quarks and gluons, referred to as partons. The structure of protons together with scale dependent behaviour of strong interaction (discussed in Section 1.1) makes the calculations of the collision evolution quite complex.

The parton scattering process with highest momentum transfer in a proton-proton collision is referred to as **hard-scattering**.

Simmilarly as an electric-charged particle can emit photons, scattered and created color-charged objects can emit gluons. Both emissions can happen in every part of a collision and, depending on the time-scale, is referred to as QED or QCD **initial and final state radiation** (ISR/FSR) if the radiated object is a photon or gluon respectively. The radiated objects can further split to lepton or quark pairs or radiate to form showers of outgoing partons (parton showers).

Due to large parton density, more than one pair of partons can collide during 1 proton-proton collision. This is referred to as multiple parton-parton interactions and is characterized by typically lower momentum transfer than the hard-scattering. The additional energy flow in the event is usually reffered to as **underlying event**. The underlying event is commonly defined as everything except hard-scattering.

After a collision, the event evolves downwards in the momentum scale, and follows the corresponding behaviour of α_s (discussed in Section 1.1). As the partons leave the interaction point, they reach the scales of order of 1 GeV, in which QCD becomes strongly interacting. In this region, partons are immediately confined to hadrons during a **hadronization** process. The resulted final state particles which come from the underlying event contaminate the measurement of the resulted final state particles from the hard scattering.
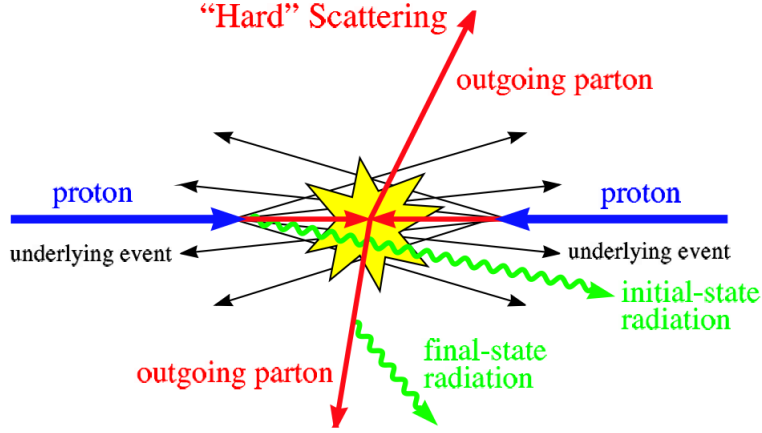
Figure 1.5: A schematic picture of important processes in a proton-proton collision [9].

According to the amount of transferred momentum, the processes during a proton-proton collision (depicted in Figure 1.5) are classified to be either hard or soft. The QCD allows to calculate both soft and hard processes. However, while the hard-scattering can be calculated perturbatively, the soft processes (UE, hadronization) require non-perturbative calculations, which are currently much less well understood, and are represented by specific models. Lets start with discussion of the calculation of hard-scattering.

Calculation of hard processes

Let A and B be the hadrons coming into collision and a and b the colliding partons, respectively. The hadronic production cross section in a hard-scattering of hadrons A and B can be defined by a factorisation theorem [10] as a convolution of partonic cross section with the parton distribution function, as:

$$\sigma(s)_{AB \to X_n} = \sum_{ab} \int dx_1 dx_2 f_a(x_1, \mu_F^2) f_b(x_2, \mu_F^2) d\hat{\sigma}_{ab \to X}(x_1 x_2 s, \mu_F^2, \mu_R^2) \qquad (1.3)$$

The factorisation theorem says, that for suficiently inclusive observables the cross section is given by contribution of parton distribution function and partonic cross section, where:

- The partonic cross setion of partons a and b is defined as:

$$d\hat{\sigma}_{ab \to X_n}(x_1 x_2 s, \mu_F^2, \mu_R^2) = |\mathcal{M}_{ab \to X_n}(x_1 x_2 s, \mu_F^2, \mu_R^2)| d\Phi_n, \qquad (1.4)$$

where μ_R is the renormalisation scale, which represents the scale dependence of the interaction, μ_F is the factorisation scale, which represents the protons scale for different transferred momentum, $\mathcal{M}_{ab \to X_n}$ is the matrix element of a studied physical process, which can be calculated from corresponding Feynman diagrams, n is the number of produced particles and $d\Phi_n$ is an element of the Lorentz invariant phase space of the final state particles, defined as:

$$d\Phi_n = \delta^4 \left(p_a + p_b - \sum_{i=1}^{n} p_i \right) \prod_{i=1}^{n} \frac{d^3 \vec{p}_i}{(2\pi)^3 2E_i}, \qquad (1.5)$$

where p_a and p_b are the initial-state momenta.

- The parton distribution function $f_a(x, Q^2)$ is defined as a probability density to find a quark with momentum fraction x in its mother proton A. Parton distribution functions at certain fixed low momentum scale Q_0 are determined phenomenologically by comparing wide range of hard scattering measurements to QCD prediction. The proton structure is not computable from the first principles, but once known for a certain scale $f_a(x, Q_0^2)$, the $f_a(x, Q^2)$ for different scales can be determined using Dokshitzer-Gribov-Lipatov-Altarelli-Parisi (DGLAP) evolution equations [10].

The formula 1.3 can be further modified, substituing 1.4 and assuming that both hadrons are protons:

$$\sigma_{pp \to X_n} = \sum_{ab} \int dx_1 dx_2 f(x_1, \mu_F^2) f(x_2, \mu_F^2) |\mathcal{M}_{ab \to X_n}| d\Phi_n. \tag{1.6}$$

The formula 1.6 for the cross section of a given process $ab \to X_n$ in a proton-proton collision holds to all orders in perturbation theory [11]. The prediction can be made for any process at any energy, which can be even beyond the current energy range and even beyond the Standard Model. This makes the factorisation theorem a powerfull tool for experimental particle physics.

1.3.1 Monte Carlo event generators

Calculation of the event evolution from the initial stage of a collision up to the final state particles and their momenta together with the hadronic cross section is useful to plan analysis strategies (a procedure to select signal over usually overwhelming background in the detector). It also gives a crucial input for new detector development.

Monte Carlo (MC) event generators [11] are software instrumets to generate high energy particle physics events. The output of such generator is a list of objects (final state particles, together with their momenta) with production cross section as they come from a proton-proton collision to the detector. The HepMC [21] event record is used by majority of MC generators. The measurements of MC generated events without any detector simulation are referred to as *particle level* measurements, contrary to *detector level* measurements, where the measured objects are reflections of final state particles as reconstructed by the detector and where detector effects, such as limited resolution and acceptance, take place. According to the processes in a proton proton collision, there are the following steps to be simulated in MC generators:

1. Hard scattering, in which the partonic cross section is defined by specific matrix element and produce few outgoing particles

2. Secondary interactions of other partons than the ones in the hard scattering

3. Parton showers associated with the incoming and outgoing coloured partons or particles

4. Hadronization of colored final state partons

5. Decays of unstable particles

From the text above it follows, that the necessary input of MC generators are: matrix elements for given processes, measured parton distribution functions, models for parton showers, models for hadronization and models for underlying event.

There are three main multipurpose MC event generators, differing on implementation or approximation of various mentioned components: Herwig++ [12], PYTHIA [13] and Sherpa [14], which contain parton shower models, packages for hadronization and approaches for underlying event. They have many processes implemented at LO, but only few NLO calculations.

As some LHC measurements require complex selection criteria (cuts), it is necessary to model both signal and background processes precisely, beyond the first approximation. The analytic formulae not only for various LO, but also for NLO matrix elements can be evaluated in dedicated programs such as NLO parton level integrator, MCFM [15], where one can get a cross section for given cuts. Currently, some generators (MC@NLO [17], POWHEG-BOX [38]) can simulate also final partonic momenta from the matrix elements up to NLO and so give also prediction of differential spectra for given cuts. To add parton showers and hadronization, in order to give the prediction of the event evolution as described in the text above, they are interfaced to multipurpose LO generators.

1.3.2   Rivet

The results of published measurements are archived in HepData [18] database, which is an wide archive of published measurements in various output format linked together via a web page [19]. Typical analysis contains quite complex event selection. The implementation of the selection on the basis of published paper might be ambiguous. Therefore, it is desired to archive also the selection codes in a straightforward and standardized way. Such archiving is provided by the Rivet routine, which is described in the following text.

Rivet [20] (Robust Independent Validation of Experiment and Theory) is a software tool for MC-Data comparisons allowing to archive particle level analyses in C++.

As discussed in Section 1.3.1, MC generators contain different models for non-perturbative processes. In order to provide reliable theoretical predictions, MC generators should describe the experimental data in the best possible way. The procedure, which compares the generator output depending on used parameters in order to fit their values to the theory is reffered to as MC tuning. Rivet is therefore a very suitable framework for purpose of MC tuning.

The key features of Rivet are:

- Independence of MC details: MC generators often differ in used convention for the intermadiate states of particles in an event. To avoid problems during running the analyses on samples from different MC generators, Rivet uses final state particles as the only relevant analysis input, without information about their mother particles.

- Generator independence: Rivet uses HepMC as the only input. Therefore, any generator that has an interface to this data format can be used with Rivet.

- Simple MC data comparisons: In Rivet, the reference data can be taken directly from the HepData[18] archive. The reference histograms can also be used to automatically define the binnings of the Rivet Monte Carlo histograms.

- Easy and standardized implementation of analyses: Rivet contains predefined classes (*Projections*) for quantities and experimentable observables (e.g. missing momentum, jets and leptons), which makes the analysis implemetation straightforward.

The Rivet is used also for the purpose of the MC Plots [34] project, which allows comparison of predictions from different MC event generators online in the web application.

In the coming Rivet release (2.1.2), the SM group required the implementation of the WW and ZZ analyses. This thesis includes such implementation. It will be discussed in Chapter 3.

1.4 The ATLAS detector

This thesis focuses on diboson production in the ATLAS [22] detector at LHC at CERN. The ATLAS detector (depicted in Figure 1.6) is a complex system, allowing reconstruction of various physics objects. The detector is a cylinder with a total length of 42 m and a radius of 11 m.

The coordinate system of ATLAS is a right-handed coordinate system with the z-axis along the beamline and with the x-axis pointing towards the centre of the LHC tunnel. The pseudorapidity, η, of particles from the primary vertex is defined as:

$$\eta = -\ln\left[\text{tg}\left(\frac{\theta}{2}\right)\right], \tag{1.7}$$

where θ is the polar angle of the particle direction measured from the positive z-axis. Particles produced perpendiculary to the z-axis have $\eta = 0$. Transverse momentum, p_T, is defined as the momentum perpendicular to the LHC beam axis. The distances are defined in $\eta - \phi$ space, where ϕ is the azimuthal angle, in terms of $\Delta R = \sqrt{\Delta\eta^2 + \Delta\phi^2}$.

From innermost parts to outermost, ATLAS consists of an inner detector, electromagnetic and hadron calorimeters and muon detectors:

- The inner detector is placed closest to the interaction point and covers pseudorapidity $|\eta| < 2.5$. It is a tracking system, which consists of silicon detectors and transition radiation trackers. The silicon detectors detect the interaction of charged particles at many discrete points in a grid, and so can visualise their tracks. They also measure ionisation energy losses of particles, and so can be used to determine particle type. Good separation of π, K, p can be achieved for $p_T < 1$ GeV. The transition radiation tracker measures the transition radiation of relativistic particles and its function is to distinguish electrons from heavier particles like pions. Due to the surrounding magnetic field, the inner detector gives information about particle momenta, which can be derived from the curvature of the particle track.

- The electromagnetic and hadronic calorimeters consist of layers of high-density material, where the particles produce showers, and a sensitive detector, which measures the visible energy. The electromagnetic calorimeter measures particles interacting electromagnetically, while the hadronic calorimeters are optimized to measure particles interacting via the strong force. The ATLAS calorimeters cover $|\eta| < 4.9$.

- The outermost part of ATLAS detector is the muon spectrometer, which measures momentum and direction of muon tracks. The muon detector consists of large number of chambers designed to measure tracks of muons and triggering chambers, surrounded by magnetic field.

The important physics objects in the measurement in this thesis are high p_T leptons, neutrinos and jets. The basic principles of their interaction with detector subsystems, schematically depicted in Figure 1.7, are the following:
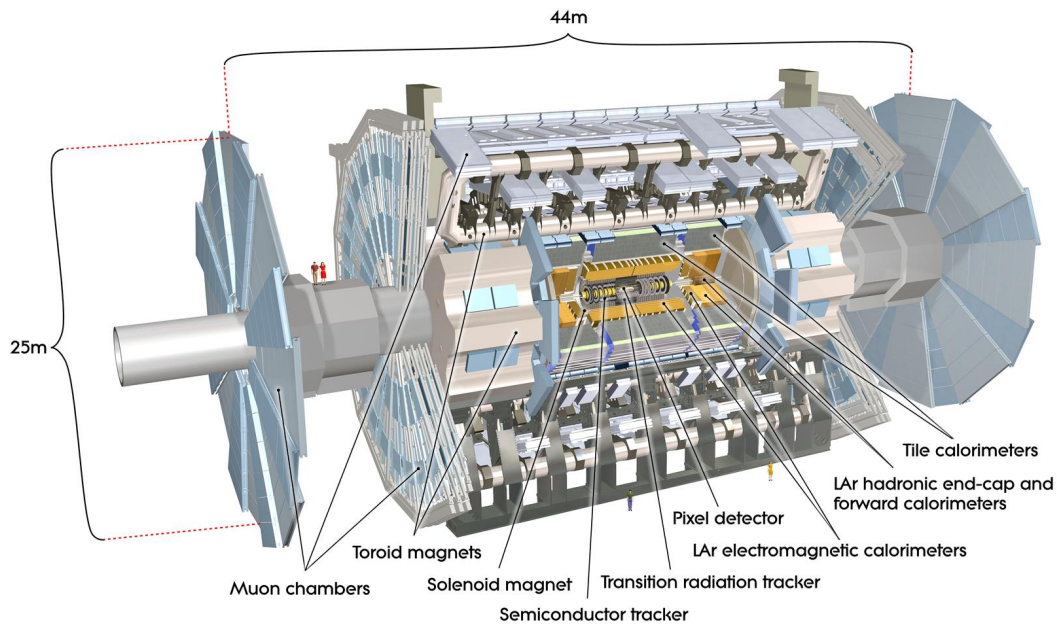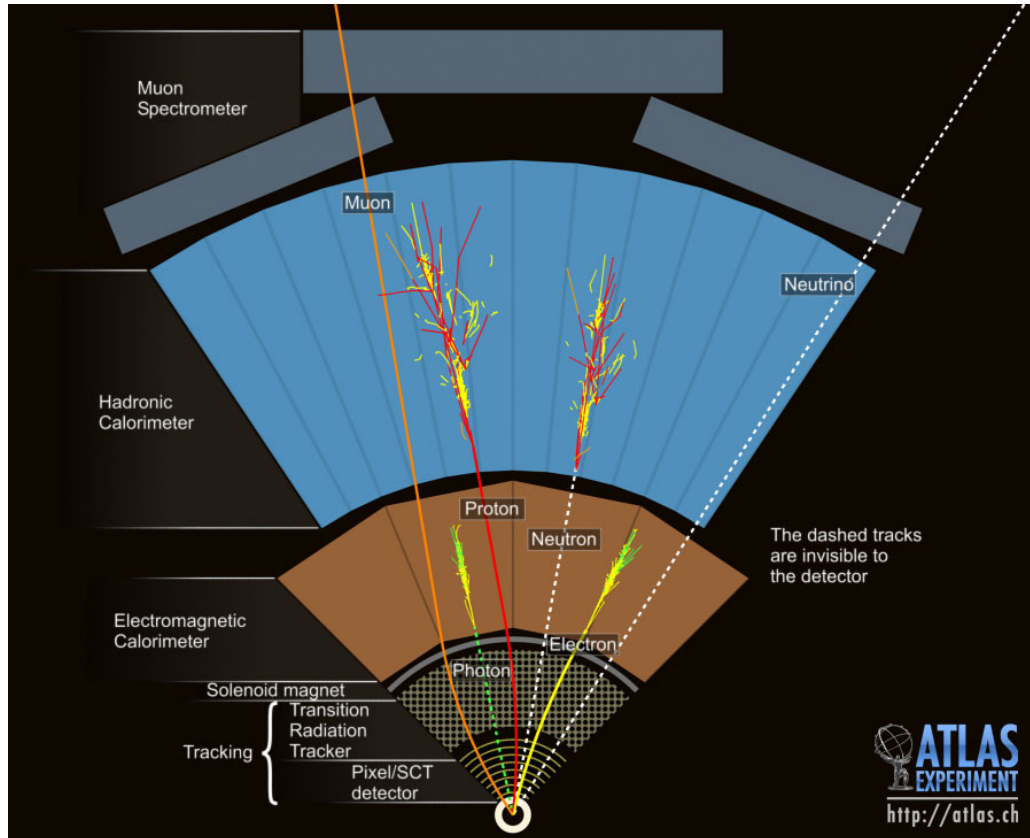
Figure 1.6: ATLAS detector and its subsystems [22].

Figure 1.7: Interaction of particles with detector subsystems [23].

High p_T leptons

The high p_T leptons to be considered in the measurement are electrons and muons. Electrons are charged particles, and therefore leave hits produced via ionization by their passage through the tracking system. They also produce an electromagnetic shower in the electromagnetic calorimeter, where they lose their energy. The electron reconstruction efficiency inside the ATLAS detector is 70-80%, depending on p_T and η, as illustrated in Figure 1.8. The efficiency for muons is slightly higher. With 200 times larger mass than electrons, muons are minimum ionizing particles. They are not stopped in the calorimeters and can be seen in the outermost muon detectors. During the passage through a detector, both electrons and muons can radiate a FSR photon. If the photon is emitted from the lepton in a direction collinear to leptons momentum, it might end in the same calorimeter cell as the lepton, and, therefore, its energy is considered to the energy of the mother lepton in the measurement. The leptons should therefore be defined in terms of a cone of electromagnetic particles, referred to as *dressed leptons*.
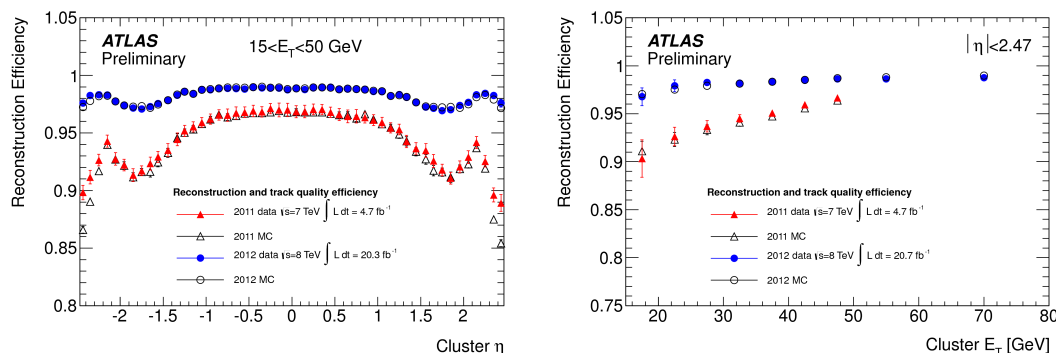
Figure 1.8: Electron reconstruction efficiency at the ATLAS detector at $\sqrt{s} = 7$ TeV and $\sqrt{s} = 8$ TeV, depending on p_T and η of the electrons [24].

Jets

Jets are collimated sprays of particles. Jets are defined by clustering detected particles together via specific algorithms. The commonly used algorithm is referred to as *Anti-kT* algorithm. It clusters particles to jets by adding their fourmomenta in a specific way, which is decided via defining two types of distances. At the beginning of the clustering, for each particle j in the event, following distances are defined:

- Distance of particle j from the beam

$$d_j = p_{Tj}^{-2} \tag{1.8}$$

- Minimum distance between particle j and every other particle i

$$d_{ij} = min(p_{Ti}^{-2}, p_{Tj}^{-2})\frac{\Delta\eta^2 + \Delta\phi^2}{R^2}, \tag{1.9}$$

where R is the parameter, which determines the size of the jet. If $d_{ij} < d_j$, the jet j is completed. If not, the fourmomentum of particle i is added to the fourmomentum

of particle j and the clustering continues by calculating all distances again with respect to existing protojets. The procedure ends, when every particle is clustered to one of the resulted jets.

Neutrinos

Neutrinos interact only via the weak force in the Standard Model. As they do not interact with any part of the detector, their presence in the event turns out as a missing energy. As the rapidity ranges covered by the central detector are restricted to $|\eta| < 4.9$, large amount of energy leaves the collision region in the longitudinal direction and cannot be used for missing energy determination. Therefore, the presence of neutrinos in an event is represented by only the missing energy in the transverse plane, referred to as missing transverse energy E_T^{miss}. However, the measured amount of missing transverse energy is increased by the measured visible energy from multiple proton-proton interactions. This increase is referred to as fake missing trasverse energy and grows as $\sqrt{n}$ with number of pp interactions, n.

Chapter 2

Diboson production

2.1 Dibosons

In this thesis, the term diboson means pair of massive electroweak bosons produced in the hard scattering. Studying diboson processes provides opportunity to test the electroweak sector of the Standard Model. Diboson production plays also important role as background in the rare processes with large missing energy, e.g. $H \to WW$ [25].

The aim of this chapter is to introduce some important terms of diboson production physics, where some details will be described only in the connection with WW production, as this work focuses mainly on the $WW \to l\nu l\nu$ process.

2.2 Diboson production cross section

In the cross section measurement, there are two important terms: fiducial cross section and total cross section. The former is a measurement in the so called fiducial phase space, which includes geometric and kinematic acceptance requirements of the detector, while the latter is a result extrapolated from the fiducial measurement.

The fiducial cross section is calculated as:

$$\sigma_{fiducial} = \frac{N_{obs} - N_{bkg}}{C \times L}, \tag{2.1}$$

where N_{obs} is the number of observed events passing selection, N_{bkg} is the number of estimated background events, C efficiency correction (the ratio of the signal event yield passing the analysis selection at the detector level to the signal event yield passing the analysis selection at the particle level), L is the integrated luminosity. The main idea to measure fiducial cross section is:

- Measure only in region of non-zero acceptance and efficiency

- Reduce model dependence of the correction factor C

The total cross section is conventionally calculated as:

$$\sigma_{tot} = \frac{N_{obs} - N_{bkg}}{A \times C \times L \times BR}, \tag{2.2}$$

where A is the detector acceptance (ratio of the signal event yield passing the analysis selection at particle level by the total number of generated signal events), and BR is

the branching ratio of the process. The total cross section measurement is useful to compare measurements from experiments with different fiducial phase region definitions (e.g. ATLAS and CMS).

Summary of Standard Model cross section measurements by ATLAS for various processes compared to theoretical predictions is given in Figure 2.1. Diboson production is a fairly rare process. As the total cross section of a pp collision at 7 TeV is $\sim$100 mb, one WW event occures in 10^{10} pp collisons.
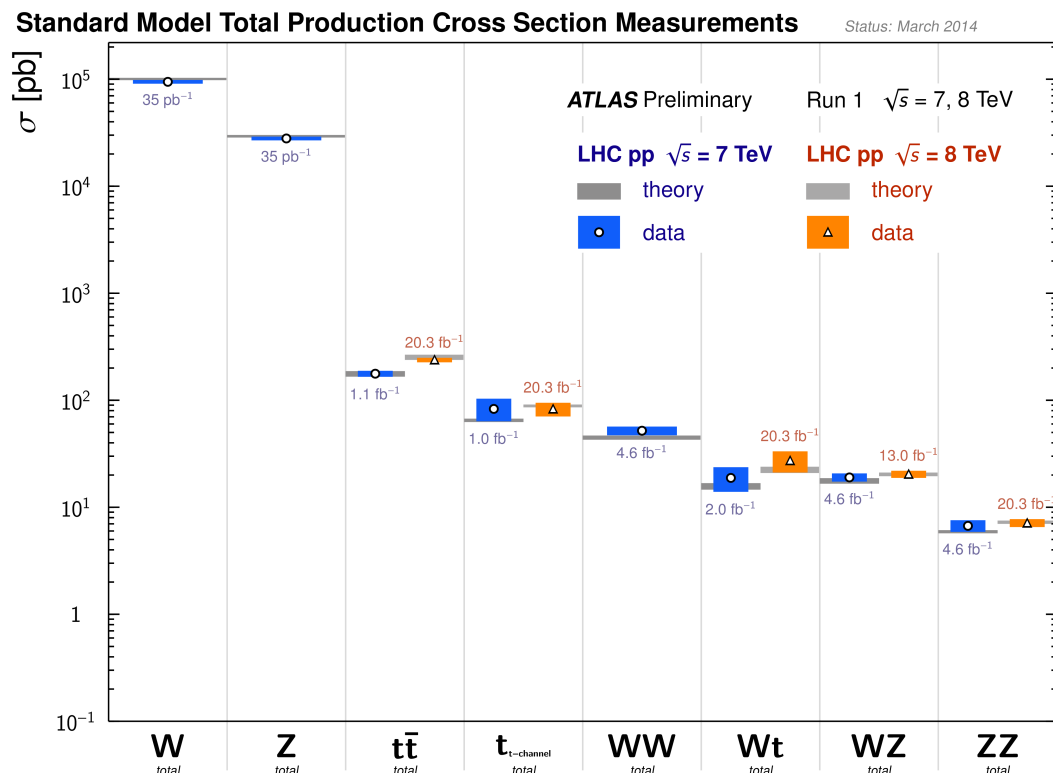

Figure 2.1: Standard Model total production cross section measurement results for various processes at the ATLAS detector at $\sqrt{s}$= 7 TeV and $\sqrt{s}$= 8 TeV [26].

The major contribution to diboson production is due to quark-anti quark scattering. Small fraction of contribution ($\sim$3%) originates from the gluon-gluon fusion. The Feynman diagrams for these processes, where both produced bosons are W, are shown in Figure 2.2.

As discussed in Section 1.3.1, the matrix elements together with final partonic momenta can be calculated to NLO in QCD, using MC@NLO and POWHEG generators, interfaced to multipurpose generators with shower and hadronisation packages, such as Herwig++, PYTHIA and Sherpa. Both NLO generators can be used for the WW signal modelling.

The ratio of the next-to leading order cross section to the LO cross section is referred to as the K-factor and is sometimes used to scale the predictions of LO generators for processes for which the NLO generator is missing and only analytic calculations are avaible.

In the measurement in this work, the NNLO contributions, initiated by the gluon-gluon fusion, are also important. Their calculation is avaible in the gg2WW [27] generator.
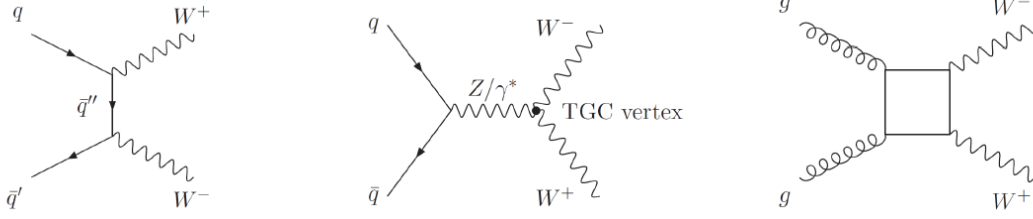
Figure 2.2: The Feynman diagrams of WW production processes. From left: quark-antiquark annihilation in the t-channel, quark-antiquark annihilation in the s-channel with a triple gauge coupling vertex, gluon-gluon fusion [28].

2.3 Diboson interactions and anomalous coupling

The s-channel vertex in Figure 2.2 is referred to as triple gauge couplig (TGC) vertex. In this vertex, interactions between three electroweak gauge bosons take place. These gauge bosons self-interactions are fundamental prediction of the Standard Model, resulting from the non-Abelian nature of the electroweak gauge theory [1]. This thesis focuses on WW production, which is sensitive to WWγ and WWZ couplings [29]. TGC vertices with charged bosons are referred to as charged TGC vertices. The effective lagrangian (assuming CP symmetry conservation and gauge invariance) for charged TGC is defined as [30]:

$$L/g_{WWV} = ig_1^V(W_{\mu\nu}^*W^\mu V^\nu - W_{\mu\nu}W^{*\mu}V^\nu) + ik_VW_\mu^*W_\nu V^{\mu\nu} + \frac{i\lambda_V}{M_W^2}W_{\rho\mu}^*W_\nu^\mu V^{\nu\rho}, \quad (2.3)$$

where g$_{WW\gamma}$=-e (electron charge), g$_{WWZ}$=-e×cotθ_W (where θ_W is the weak mixing angle of the Standard Model), V=Z/γ, V$^{\mu\nu}$= ∂_μV$_\nu$-∂_μV$_\nu$ (and the same for W$^{\mu\nu}$). In the Standard Model, the five coupling parameters have fixed values g_1^Z=1, k_Z=1, k_γ=1, λ_Z=0 and λ_γ=0 at tree level. To study anomalous (non-SM) coupling means to measure the deviation of the coupling parameters with respect to the SM predictions. In such measurements, coupling parameters g_1^V and k_V are expressed in terms of anomalous parameters Δg_1^V=1-g_1^V and Δk_V=1-k_V, respectively, and their deviations from zero value are being searched. Differencies from SM predicted values could arise from new physics, e.g. from presence of new particles, not predicted by the SM.

The cross section for given anomalous parameter depends on squared center-of-mass energy, s. Therefore, higher center-of-mass enegies can enhance the sensitivity on anomalous triple gauge coupling.The measured limits on anomalous parameters are in Figure 2.3. The precise measurement was made at LEP [31] in e^+e^- collisions. The measurement at LHC at high transferred momentum shows even more precise results.

2.4 Diboson production modes

Depending on the decay topology, bosons can decay in leptonic, semi leptonic and hadronic mode. For example, the W boson decays leptonically (in three channels: either to electron, muon or tau with corresponding neutrino) and hadronically. The measured [5] hadronic branching fraction of a W boson is approximately 70%, while the measured leptonic branching fraction is significantly lower, approximately 11% for each (eν, $\mu\nu$, $\tau\nu$) channel. This thesis focuses on production of W^+W^- pairs both decaying leptonically ($WW \rightarrow l\nu l\nu$),
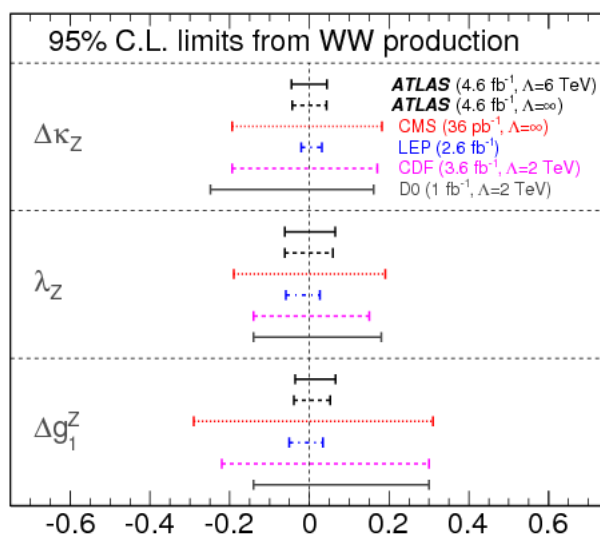
Figure 2.3: Measured limits on anomalous coupling from ATLAS, CMS, CDF, D0, and LEP experiments [29].

with four final state combinations ($e^-\bar{\nu}e^+\nu$, $\mu^-\bar{\nu}\mu^+\nu$, $e^-\bar{\nu}\mu^+\nu$, $\mu^-\bar{\nu}e^+\nu$). The leptonic branching fraction of a WW boson pair for one final state combination is 11%×11%. Since there are four final state combinations, the branching fraction for $WW \rightarrow l\nu l\nu$ processes is 4×11%×11%=4.8%. Tau decays contribute very little.

2.4.1 Beyond the zero-width approximation

In the zero-width approximation, the intermediate unstable particle state is restricted to the mass shell. This is, however, only an approximation and in particular in the threshold region it is not sufficient. Rather, one has to describe the W bosons as resonances (with a Breit-Wiegner distribution), with a finite width so as to avoid singularities inside the physical phase space, and analyse their presence through their decay products $l^+l^-\nu\bar{\nu}$. Processes in Figure 2.4 a) involve two W bosons and are a first step beyond the zero-width approximation. However, these are not the only processes which contribute to the four fermion final state. There are also contributions from processes with the same initial and final states, but different intermediate states as shown in Figure 2.4 b). They are denoted as singly-resonant graphs and are included in POWHEG generator. The contribution of singly-resonant diagrams is usually small, but can be enhanced in certain regions of phase space [16].
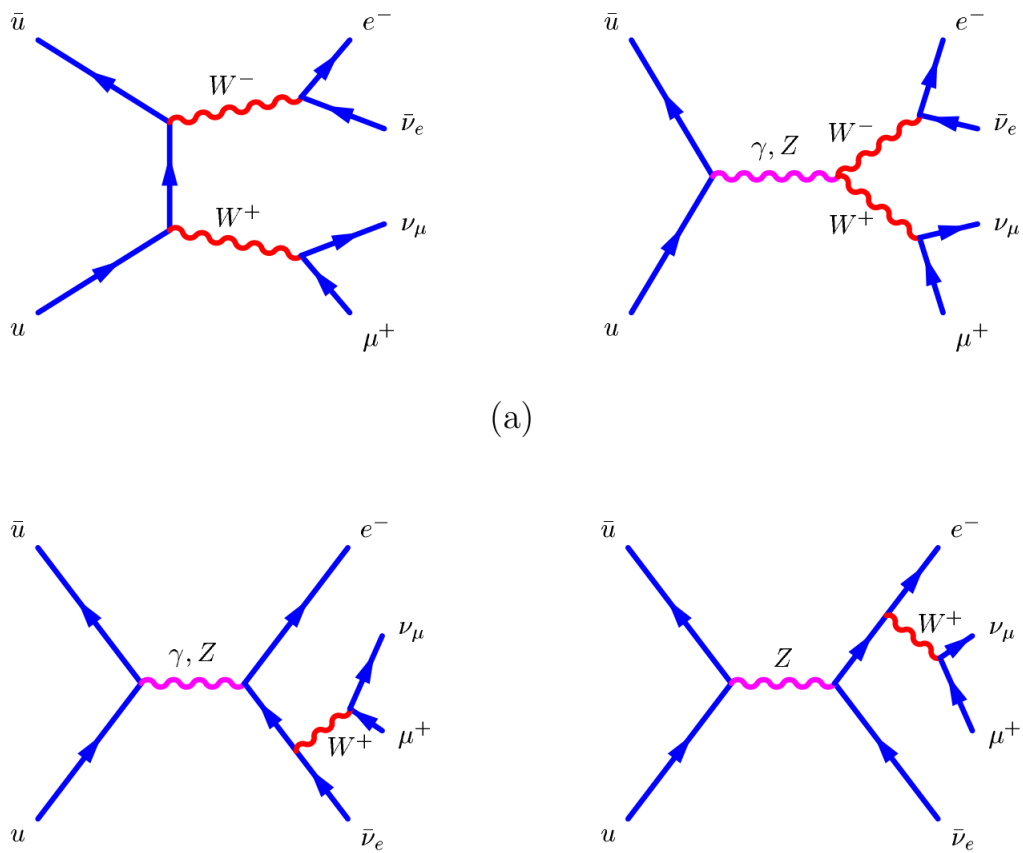
Figure 2.4: The diagrams contributing to the parton-level process $q\bar{q} \rightarrow e^-\bar{\nu}_e\nu_\mu\mu^+$ [16]. (a) Doubly resonant diagrams. (b) Singly resonant diagrams.

Chapter 3

WW and ZZ analyses and Rivet

WW production cross section has been measured by ATLAS at 7 TeV and the results were published in paper [29]. The aim of this project is to describe the measurement strategy from this paper and to reproduce the selection at generator (particle) level, in order to further implement this analysis (and analogous ZZ analysis published in paper [32]) in Rivet. In the first two Sections of this Chapter, the signal and background processes of the WW measurement will be defined. Then, the corresponding object selection at detector level and fiducial region definition will be discussed. Finally, the reproduction of such event selection at particle level together with Rivet analysis implementation will be presented. In the remaining part of this Chapter, the ZZ measurement strategy and implementation in Rivet will be shown.

3.1   Signal

The given WW analysis focuses on production of W^+W^- both decaying leptonically ($W^+W^- \to l^- \bar{\nu} l^+ \nu$). The signal consists of two oppositely charged leptons and missing transverse energy from the two neutrions. The considered final state can be any combination of e and μ, including cascade decays of τ. Therefore, the signal is divided into three channels:

- Same-flavour channel with two e and missing transverse energy

- Same-flavour channel with two μ and missing transverse energy

- Opposite-flavour channel (one e and one μ) and missing transverse energy

3.2   Background

As discussed in Chapter 2, WW production is a rare process. In the collected data, there are numerous other processes (mostly with larger cross section), giving simmilar final state experimental signatures as WW leptonic decays, which must be eliminated. Such other processes are referred to as background processes and such elimination is referred to as selection. Basically, the simmilar experimental signatures are caused by one or both of the following reasons:

- The background process leads to the same final state as the signal process, with some additional leptons or jets. An event with such additional objects must be vetoed in the measurement. However, if these additional physics objects do not fall

to the detector acceptance, they are not visible in the measurement. The remaining measured leptons and missing energy fake the signal.

- The background process leads to different final states than the signal process, but some objects of these final states are misidentified as the signal physics objects in the detector. For example, a jet can in some cases be misidentified as lepton and at the same time missing energy can be added from multiple proton-proton interactions in the event.

In WW measurement, the main sources of background are: Drell-Yan process, $t\bar{t}$ production, single t production, W+jets production, and production of other dibosons.

The Drell-Yan process, shown in Figure 3.1(left), is represented by Z or γ boson decays with associated 0 or more jets. As the Z/γ boson produce two same flavor opposite sign leptons, together with fake missing energy from multiple proton proton interactions (discussed in Section1.3), this process can lead to the same experimental signature as WW. Since the Drell-Yan process has 1000 times larger cross section than WW production, as seen from the Figure 2.1, it can significantly affect the measurement. Since Z/γ bosons decay to two leptons of the same flavour, Drell-Yan process contaminates mainly the same-flavour channel, but also contributes to the opposite flavor channel through the cascade tau decays.

The top producion, dominated by top-anti top production, as shown in Figure 2.1(right), has 3.5 times larger cross section than the signal. As seen in Figure 3.1, $t\bar{t}$ production leads to the same final state as signal, but contains additional b-jets. If both jets do not fall to the detector acceptance, the process can mimic the WW event. Vetoing events with additional jets suppresses the top production considerably, however.

In case of W+jets process, one jet can be misidentified as lepton and so fake signal together with fake missing energy.

The contributions from various background processes to the collected data in the dilepton mass distribution in electron channel is illustrated in Figure 3.2. They can be eliminated by applying various object and event selection criteria, which will be described in the following text.
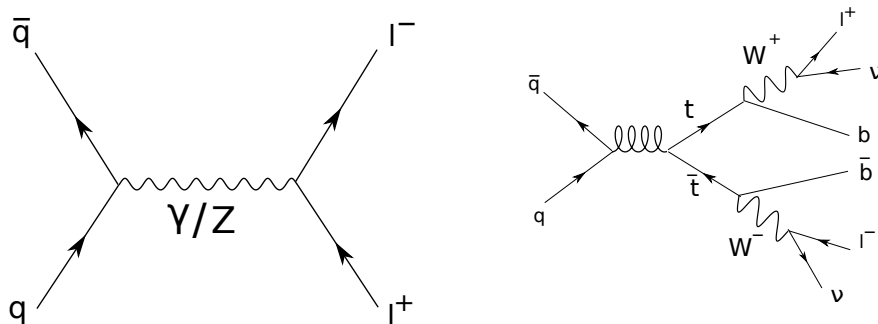

Figure 3.1: Selection of processes which contribute to the dominant background processes in the WW measurement. Left: Drell-Yan process. Right: $t\bar{t}$ production.
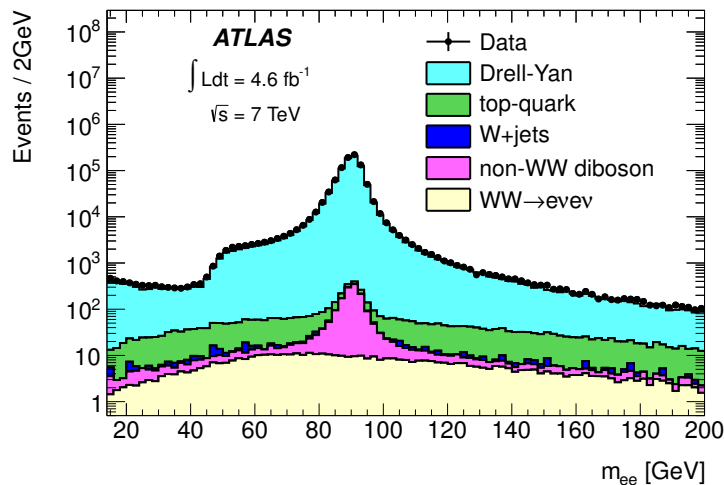
Figure 3.2: Comparison between data and simulation for the dilepton invariant mass distribution for the ee channel. The contributions from various background processes are estimated using MC simulation. Taken from [29].

3.3   WW object selection at detector level

In this Section, the object selection for WW measurement at the detector level, as developed in paper [29], will be reviewed for completness, because the particle level measurement is based on the detector level selection.

3.3.1   Analysis objects

The important analysis objects (leptons, jets and neutrinos) are searched in the η-ϕ space of the coordinate system of the ATLAS detector, as discussed in Section 1.4.

Leptons

Electrons are reconstructed from a combination of an electromagnetic cluster in the calorimeter and a track in the inner detector. Muon candidates are reconstructed in the inner detector and the muon spectrometer.

The first and second highest p_T lepton in an event is referred to as leading and subleading lepton, respectively. The leading lepton transverse momentum is required to be $p_T > 25$ GeV, the subleading is required to be $p_T > 20$ GeV. In order to cover the detector acceptance, cuts are applied also at the lepton pseudorapidity. The muon pseudorapidity is required to be $|\eta| < 2.4$. For electrons $|\eta| < 2.47$, excluding the transition region between the barel and endcap calorimeters ($1.37 < |\eta| < 1.52$).

Jets

Jets are reconstructed from topological clusters of energy in the calorimeter by Anti-k_t algorithm with $R = 0.4$. In order to cover the detector acceptance, the clustered object is referred to as jet if it has $p_T > 25$ GeV and $|y| < 4.5$.

Missing transverse energy

As discussed in Section 1.4, the neutrinos are experimentally observed as missing transverse energy in the detector, E_T^{miss}, which is calculated from the momentum imbalance.

In order to avoid increase of missing energy from mismeasured leptons or jets in the measurement on data, the missing energy is represented by a missing energy relative quantity:

$$E_{T,Rel}^{miss} = \begin{cases} E_T^{miss} \times \sin(\Delta\phi) & \text{if } \Delta\phi < \pi/2 \\ E_T^{miss} & \text{if } \Delta\phi > \pi/2 \end{cases}$$

where $\Delta\phi$ is the difference in the azimuthal angle between the $\vec{E}_T^{miss}$ and the nearest (in terms of δR lepton or jet.

3.3.2 Overlap removal

To avoid reconstructing one analysis object as two or more different objects in the detector, the overlap removal procedure is applied. The most important is jet/e overlap removal. By construction, any electron object detected in the calorimeter can also be clustered to the jet object. For this reason, any jet within $\Delta R < 0.3$ from an electron is removed from the selection.

The FSR photon emmited by muon might be misreconstructed as an electron, if the photon converts to e$^+$e$^-$ pair. Therefore, the overlap removal procedure is applied on electrons and muons within $\Delta R < 0.1$, the electron is removed. This procedure is also applied on electron pairs within $\Delta R < 0.1$, where the electron with lower p_T is removed.

3.3.3 Fiducial region definition

The fiducial region used in the WW cross section measurement is, by the analysis object selection, defined as:

- Dressed leptons $\Delta R = 0.1$

- p_T of leptons > 20 GeV

- p_T of leading lepton > 25 GeV

- η of electrons: $|\eta| < 1.37$ OR $1.52 < |\eta| < 2.47$

- η of muons: $|\eta| < 2.4$

With further criteria, applied in order to eliminate the contributions from background processes (which will be explained in the next section):

- Exactly two oppositely charged leptons

- Dilepton mass $m_{ll} > 15$ (10) GeV for the same (opposite) flavour channel

- $|m_{ll} - m_Z| > 15$ (0) GeV for the same (opposite) flavour channel, where m_Z is the mass of the Z boson

- $E_{T,Rel}^{miss} > 45$ (25) GeV for the same (opposite) flavour channel

- No Anti-k_T jets ($R = 0.4$) with $p_T > 25$ GeV in $|y| < 4.5$ satisfying $|\Delta R(jet,e)| > 0.3$

- p_T of dilepton system > 30 GeV

3.4 WW selection at particle level

As discussed in Section 1.3.1, to plan selection strategies and determine theoretical predictions, MC generated events are used. The event selection on MC samples is referred to as selection at particle level. In the remaining text of this Chapter, particle level WW selection procedure will be illustrated on MC generated signal samples together with Drell-Yan and $t\bar{t}$ background contributions. The selection was realized in Root [33] on D3PD samples with root nTuples according to the selection outlined above. The samples were prepared by the ATLAS SM group and are described in detail in the Internal Note [36]. The contribution of various signal and background samples were appropriatly normalized to cross section and added to predict yields corresponding to collected luminosity of 4.6 fb^{-1}.

3.4.1 Particle level analysis objects

At the particle level, the fiducial phase space is defined by selection criteria similar to those used at detector level. This minimizes the dependence of correction factor C (see Chapter 2) on MC. Therefore, the object selection is the following:

Leptons

The lepton definition is the same as in Section 3.3.1. As discussed in Section 1.4, the FSR photon can fall to the same calorimeter cell, if it is emmited collineary with the electron, and so contributes to its measured energy. Therefore, during the selection, leptons clustered together with photons in a cone of radius R (*dressed leptons*) are used. In this measurement, lepton kinematics account for photon contributions within ΔR=0.1.

Jets

Generator level jets are reconstructed by Anti-k_t algorithm with $R = 0.4$ from all objects which contribute to the jet definition at the detector level, e.g. all final state particles, except muons and neutrinos. Jets are reconstructed in the same restricted p_T and η range, as defined in Section 3.3.1.

Missing transverse energy

In the hadron level analysis, as we have information about neutrino kinematics, the missing transverse energy is calculated directly from the fourvectors of the final state neutrinos. The relative missing transverse energy is defined as in Section 3.3.1.

3.4.2 MC samples

In the analysis, the main contribution to WW production, from initial states with two incoming quarks, is simulated by the MC@NLO. For the gluon contribution to WW production the gg2ww generator is used. The Drell-Yan background is modeled by ALPGEN [35], $t\bar{t}$ production is simulated with MC@NLO. The parton showers and underlying event are modelled using HERWIG and JIMMY. A full list of signal samples, their cross sections and k-factors is given in the internal Note [36].

3.4.3 Signal selection

In conformity with the considered leptonic WW final states, only events with exactly two oppositely charged leptons (electrons or muons) (in p_T and η ranges as discussed in Section 3.4.1) are accepted. After this selection, if we look at the dilepton mass distribution in Figure 3.3, we can see, that the dominant background is the Drell-Yan process. To reduce this background and background from the $t\bar{t}$ production, there are following steps applied in the selection:

1. The Drell-Yan contributions are different for the opposite and same-flavour channel. Therefore, the corresponding strength of selection criteria is also differs between both channels. In the same-flavour channel, the significant contribution of Drell-Yan background is removed by rejecting events with dilepton mass close to the Z mass (15 GeV window). To reduce the Drell-Yan contribution in the low dilepton mass region, the dilepton mass is required to be greater than 15(10) GeV in the same (opposite) flavour channel.

2. After previous cut, as the Drell-Yan process is characterised byl a low missing energy, if we look at the $E_{T,Rel}^{miss}$ distribution in Figure 3.4., we can see a significant contribution of Drell-Yan background in the low $E_{T,Rel}^{miss}$ region (again mainly in the same-flavour channel). The Drell-Yan background is further reduced by rejecting events with low $E_{T,Rel}^{miss}$ in both same and opposite flavor channels. To pass this selection, the missing trasverse energy of an event is required to be $E_{T,Rel}^{miss} > 45$ (25) GeV for the same (opposite) flavour channel.

3. After applying the previous criterium, the dominant background is the $t\bar{t}$ production. As this process is charecterized by the same final state as signal with additional jets, it is reasonable to look at the jet multiplicity distribution. The $t\bar{t}$ background is estimated by vetoing events with at least one jet. Only the contribution in zero jet bin in Figure 3.5 remains for further selection.

4. After the previous step, no specific background dominates. However, in the detector-level measurement (as shown in Figure 3.6), the multiple proton-proton interactions add the Drell-Yan contributions in the low p_T domain of the lepton pair. This effect is reduced by requiring lepton pair $p_T > 30$ GeV. To reach agreement with the detector level selection, this requirement is therefore also applied at particle level.

3.4.4 WW production cross section at particle level

After applying selection criteria, the fiducial cross section can be calculated. The measured fiducial cross section per channel is shown in Table 3.1. The results are in good agreement, the difference is within 2%. The expected yield at integrated luminosity of 4.6 fb $^{-1}$ is approximately 1550 WW events.

The resulted normalized differential fiducial cross section ($1/\sigma_{WW}^{fid} \times d\sigma_{WW}^{fid}/dp_T$) in the leading lepton p_T spectrum together with results from data from HepData archive is depicted in Figure 3.7. In the normalized distribution, the systematic uncertainties of the distribution and of the normalization factor cancel. The cross section uncertainties are dominated by the statistical uncertainties [36]. This means, that the next measurements with more data should be more precise.

As seen in Figure 3.8, the presence of anomalous TGC is expected to enhance diboson production rate. The significant increase is expected to be observed in the high pT tail of leading lepton p_T distribution.
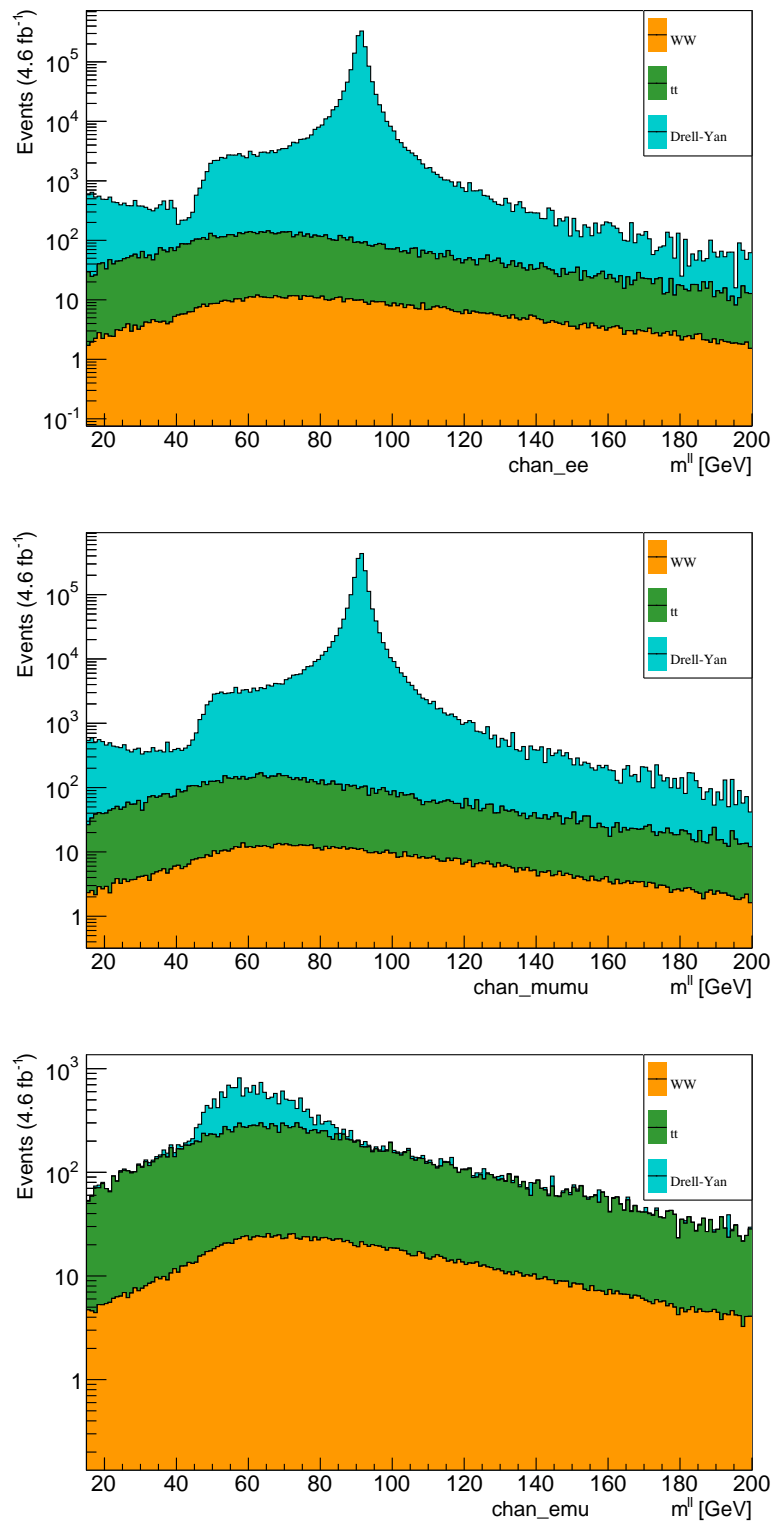
Figure 3.3: The invariant mass distribution of the lepton pair in all channels before applying the dilepton invariant mass, m_{ll}, selection criteria. It is obvious, that in the opposite flavor channel, the contribution of the Drell-Yan process is significantly smaller than in the same flavour channel.
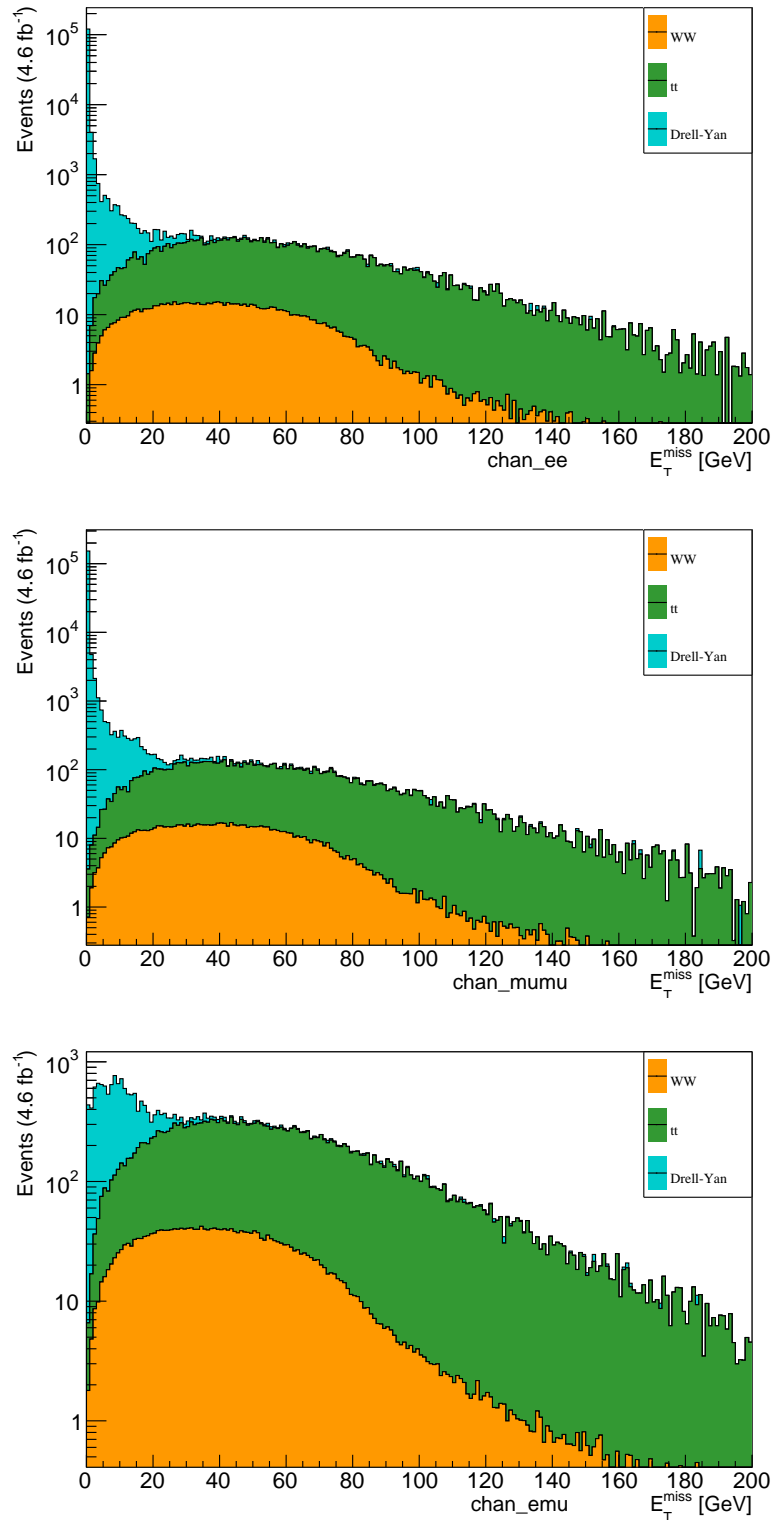
Figure 3.4: Missing energy distribution in all channels before applying the missing energy selection criteria.
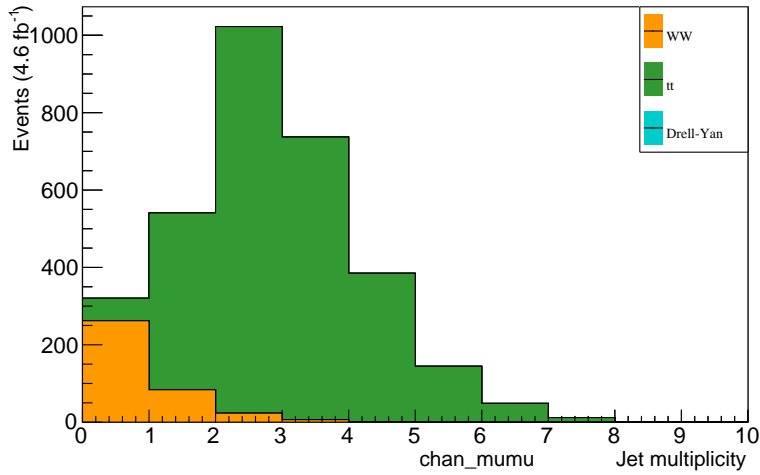
Figure 3.5: Jet multiplicity in the $\mu\mu$ channel before applying the jetveto cut. After the selection, only the zero bin remains.
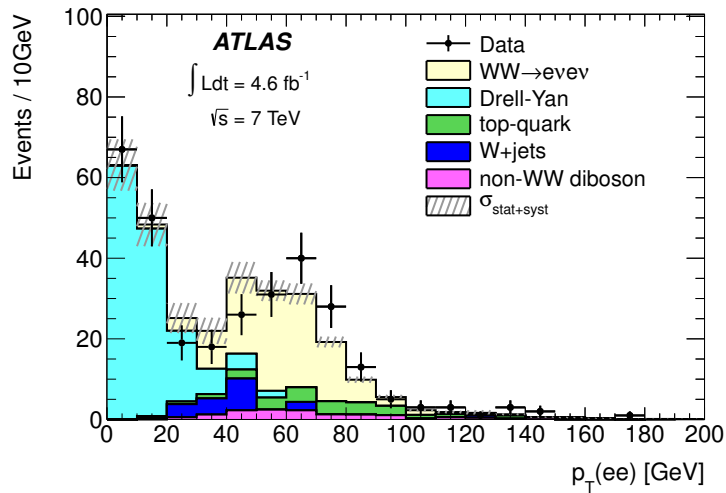

Figure 3.6: Transverse momentum of the lepton pair in the ee channel before applying the corresponding cut [29].

Channel	σ_{fid} [fb]	$\sigma_{fid}^{Article}$ [fb]
ee	53.5 ± 0.5	54.6 ± 3.7
$\mu\mu$	57.9 ± 0.5	58.9 ± 4.0
$e\mu$	228.5 ± 1.1	231.4 ± 15.7

Table 3.1: The measured fiducial cross section σ_{fid} for the three channels separately (with statistical uncertainty) in comparison with the results [29] $\sigma_{fid}^{Article}$ (with statistical and total theoretical uncertainty added in quadrature).
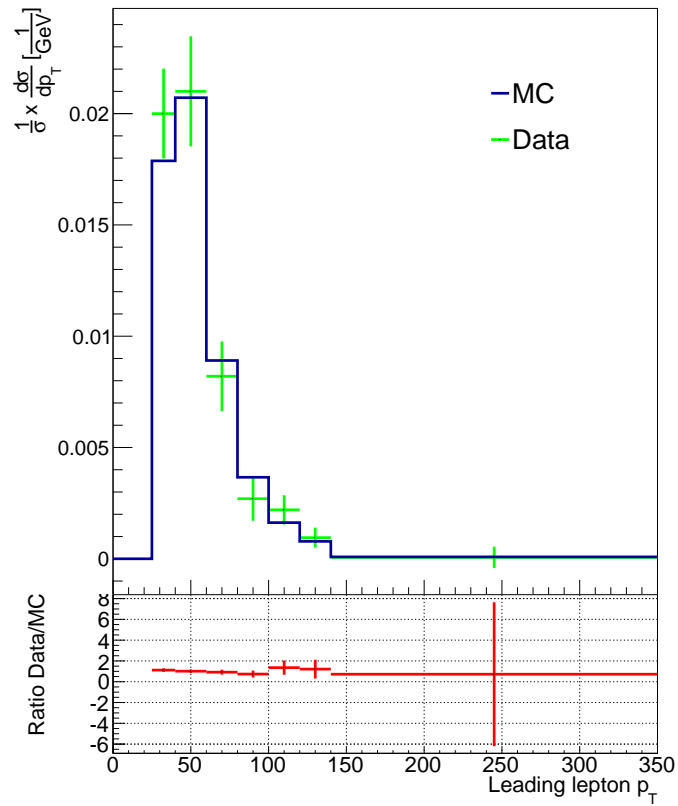
Figure 3.7: The measured normalized production cross section as a function of the transverse momentum of the leading lepton.
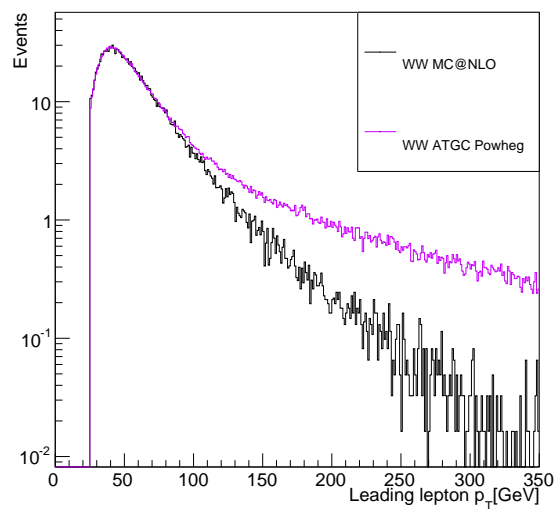

Figure 3.8: The leading lepton p_T spectrum of the signal samples before applying the selection cuts from the SM prediction (simulated by MC@NLO) and from the non-SM prediction (simulated by POWHEG) with anomalous parameters Δk_W=-0.2, Δg_1^W=0.67.

3.5   Rivet WW analysis implemetation

All the parts of the offline selection at particle level described in Section 3.4 (and in the following text referred to as offline analysis) were implemented to the Rivet framework (described in Section 1.3.2). Used MC input was the same as in offline selection, which allowed direct validation of the analysis. In this Section, used Rivet projections and their parameters will be discussed.

3.5.1   Analysis objects

The important objects in analysis were defined by specific Rivet projections in following way:

Jets

In conformity with the offline selection, jets were found between all final state particles, except muons and neutrinos, by Anti-k$_T$ algorithm with R=0.4. The jet reconstruction was made by a Fastjet projection, which interfaces general jet algorithm library FastJet [37].

Leptons

Leptons were defined by the DressedLeptons projection, where the photons are added to the lepton fourmomentum in the same way as in the offline analysis, i.e. if they are located in the cone around photon of radius $\Delta R = 0.1$. Photons from hadron decays were not included in dressing. The leptons were found in the same restricted p_T and η ranges, as in the offline selection.

Neutrinos

Neutrinos were found by the MissingMomentum projection, which calculates the reverse vector sum of visible momentum (i.e. excluding neutrinos). The relative missing energy requirement was defined as in the offline selection.

3.5.2   Selection and results

All the selection criteria discussed in Section 3.4.3 were implemented also to the Rivet routine. The results from Rivet are in good agreement, especially in the differencial spectrum of leading lepton p_T. The normalized differential fiducial cross section in bins of the leading lepton p_T is depicted in Figure 3.9. All the features seen in the reference plot are seen also in the Rivet plot. There are some small differencies between the result from Rivet and from paper [29] in the fiducial cross section per channel (1% for $\mu\mu$ channel and $e\mu$ channel and under 2% for ee channel). The total fiducial cross section in the opposite flavour and both same flavour channels compared with data from HepData are shown in Figure 3.10.

For more detailed comparison of results, Table 3.2 and Figure 3.11 show a comparison of fiducial cross section per channel from the paper [29], offline analysis and Rivet. From the ratio plots it is obvious, that the reproduced Offline analysis and the Rivet routine are in excellent agreement - the ratio is within 1%.

As outlined in Section 1.3.2, Rivet provides opportunity to compare spectra from different generators. I have generated the $WW \to l^+l^-\nu\bar{\nu}$ events in Herwig++, which allows the possibility of generating events to LO and NLO (using Powheg parton shower matching

method). Such comparison of leading lepton p_T spectra os LO and NLO events is shown in Figure 3.12.
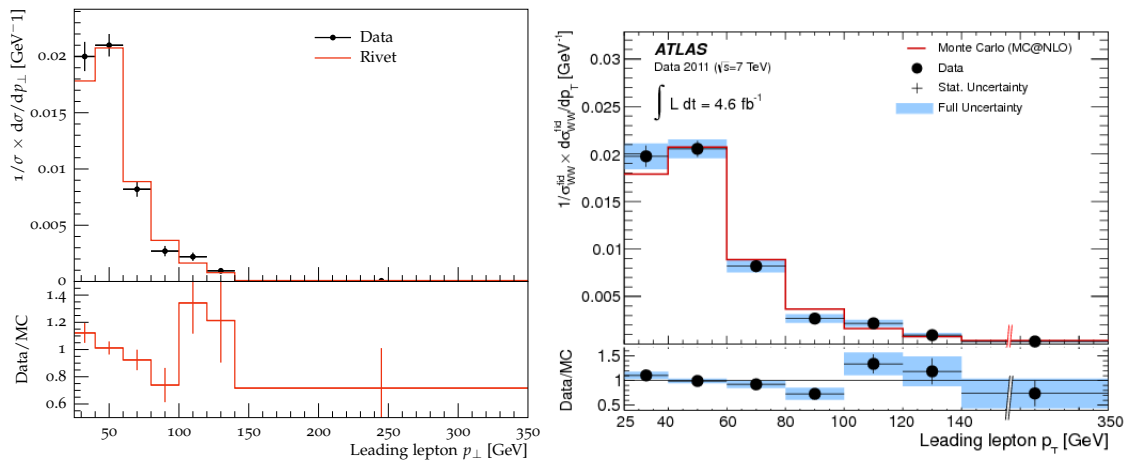

Figure 3.9: The normalized differential fiducial cross section in bins of the leading lepton p_T and Data/MC ratio. Left: The result from Rivet, plotted with data from HepData[18]. Right: The plot from [29].

channel	$\sigma_{fid}^{\text{Article}}$ [fb]	$\sigma_{fid}^{\text{Offline analysis}}$ [fb]	$\sigma_{fid}^{\text{Rivet}}$ [fb]	$\sigma_{fid}^{\text{Data}}$ [fb]
ee	54.6	53.5	53.6	56.4
$\mu\mu$	58.9	57.9	58.4	73.9
$e\mu$	231.4	228.5	229.6	262.3

Table 3.2: Comparison of WW production cross section results from the paper [29] $\sigma_{fid}^{\text{Article}}$, from the offline analysis presented in Chapter3 $\sigma_{fid}^{\text{Offline analysis}}$ and from Rivet $\sigma_{fid}^{\text{Rivet}}$.

3.6   ZZ analysis implemetation

Similarly as WW analysis, the ZZ measurement is important field for testing EW sector of the SM and searches for anomalous TGC. The ZZ production cross section has been measured at the ATLAS detector at 7 TeV and the results were published in paper [32]. As this analysis was not implemented to the Rivet routine before, a part of this work was to participate in such implementation. As the main topic of this thesis is the WW production, in this Section, the ZZ selection will be presented in less detail, than the WW selection.

3.6.1   ZZ selection and analysis objects

There are two processes considered in this analysis. The former is the process with two Z bosons decaying to electrons or muons, where one Z can be offshell ($ZZ^{(*)} \to l^+l^-l^+l^-$). The latter is the process with one Z boson decaying to electrons or muons and a second Z boson decaying to neutrinos ($ZZ \to l^+l^-\nu\bar{\nu}$). The cascaded decays from τ were not included in the signal.
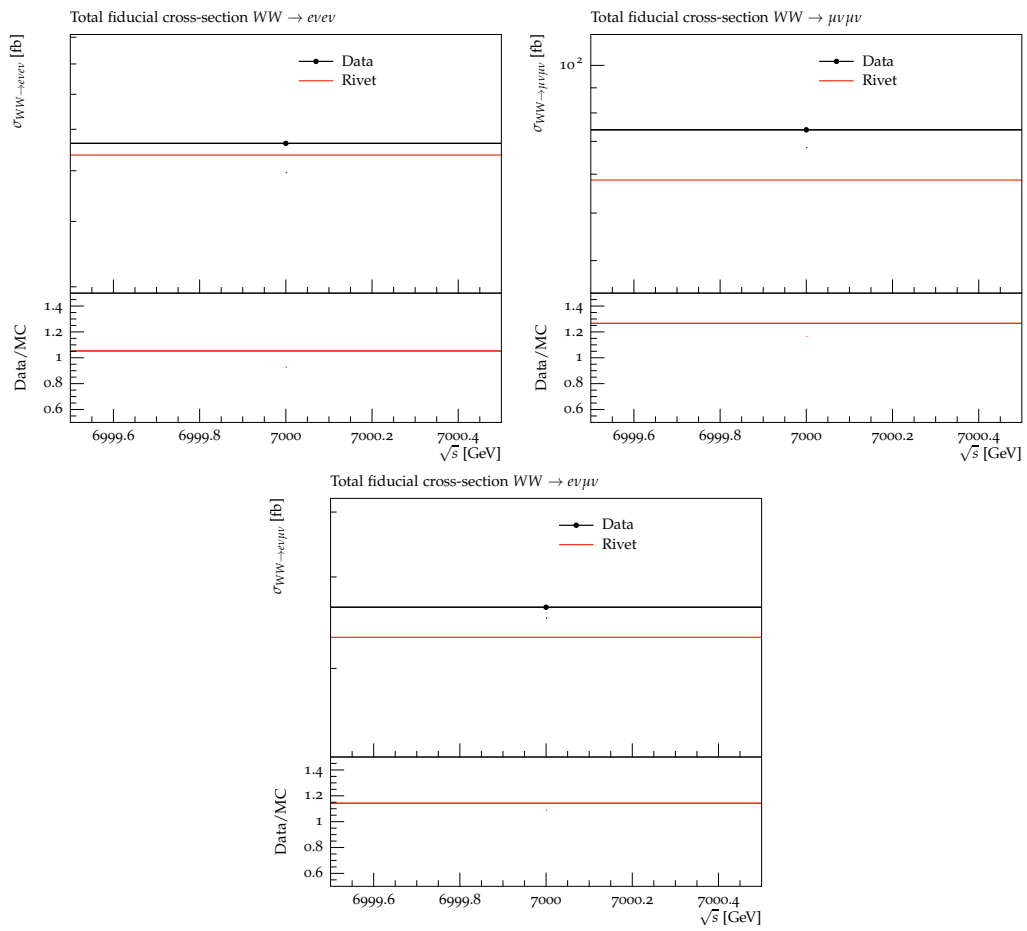
Figure 3.10: Fiducial WW production cross section in *ee* $\mu\mu$ and *eμ* channels plotted with data from HepData [18].
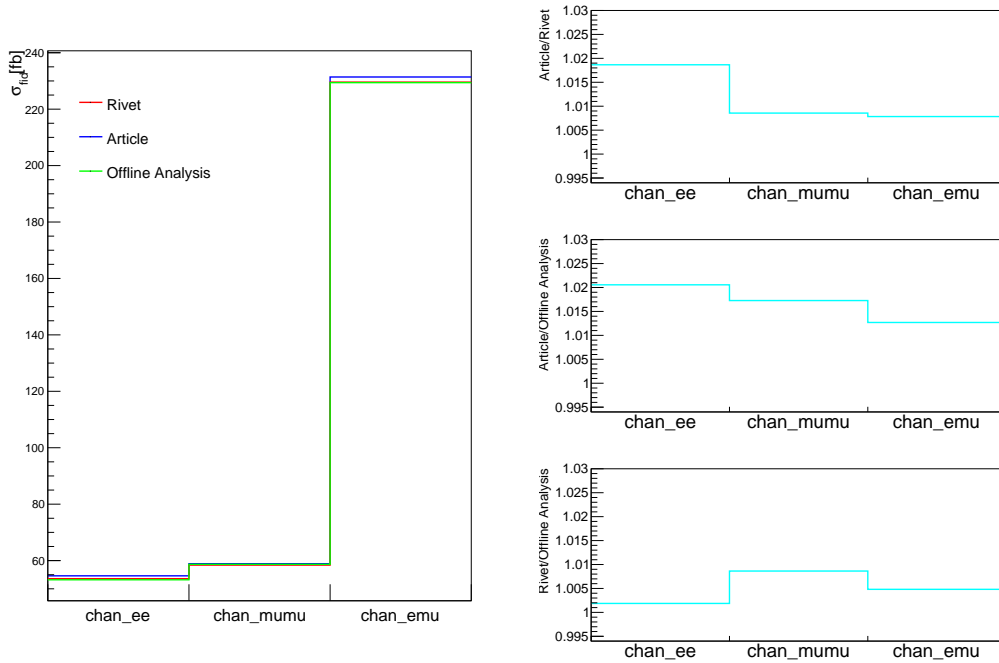
Figure 3.11: Comparison of fiducial WW production cross section results from the paper [29] $\sigma_{fid}^{\text{Article}}$, from the offline analysis presented in Chapter 3 $\sigma_{fid}^{\text{Offline analysis}}$ and from Rivet $\sigma_{fid}^{\text{Rivet}}$ and corresponding ratio plots.
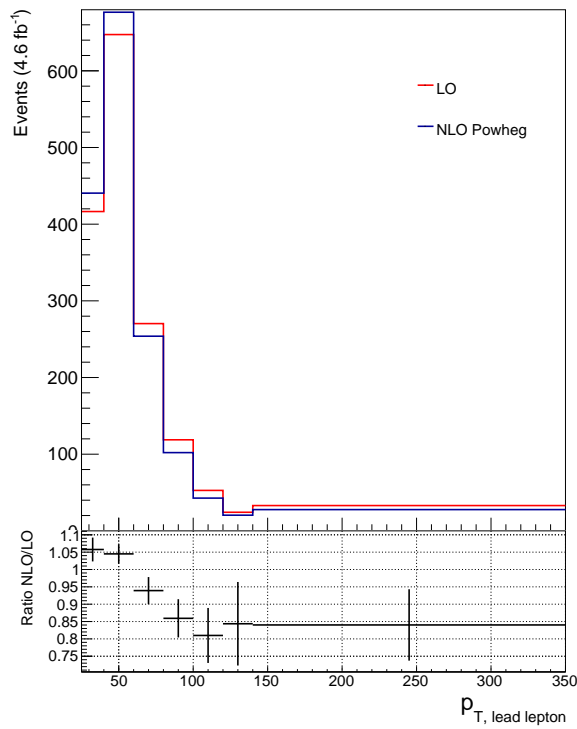

Figure 3.12: Comparison of LO and NLO leading lepton p_T spectra.

The objects in ZZ analysis were found using the same Rivet projections classes as in the case of WW analysis in Section 3.5. In both processes, the fiducial region contains 2 opposite sign dressed leptons ($\Delta R = 0.1$) in restricted p_T and η ranges. The fiducial selection has the following specific requirements for both production processes:

ZZ→4l selection criteria

- Leptons separated at least by $\Delta R = 0.2$

- $p_T^l > 7$ GeV, $|\eta^l| < 3.16$

- Dilepton invariant masses within the Z mass window:

  - For ZZ both Z $66 < m_{ll} < 116$ GeV
  - For ZZ^* Z: $66 < m_{ll} < 116$ GeV, Z*: $m_{ll} > 20$ GeV

- Ambiguities in pairing leptons to a Z boson are resolved by choosing the combination that results in the smaller value of the sum $|m_{ll} - m_Z|$ for the two pairs

ZZ→2l2ν selection criteria

- Leptons separated at least by $\Delta R = 0.3$

- $p_T^l > 20$ GeV, $|\eta^l| < 2.5$

- Dilepton invariant mass: $76 < m_{ll} < 106$ GeV

- Dineutrino invariant mass: $66 < m_{\nu\bar{\nu}} < 116$ GeV

- No particle level jets with $p_T > 25$ GeV in $|y| < 4.5$ (Jets defined by Anti-k_T algorithm with $R = 0.4$)

- Axial MET: $\frac{-p_T^{\nu\bar{\nu}} p^Z}{p_T^Z} < 75$ GeV
  (Projection of the transverse missing energy along the direction opposite to the $Z \to l^+l^-$ candidate in the transverse plane)

- Fractional p_T difference: $\frac{p_T^{\nu\bar{\nu}} - p_T^Z}{p_T^Z} < 0.4$

3.6.2   Results

To model both signal channels, the NLO generator POWHEG-BOX [38] interfaced to PYTHIA was used. The contribution from $gg \to ZZ$ were accounted for by scaling $qq \to ZZ$ by 5.75%, which was based on the resulted cross section predictions from MCFM. The resulted ZZ fiducial cross section for all three production processes is in Table 3.3. We can see a good agreement between the results. The difference is within 2%. The expected yield at integrated luminosity 4.6 fb $^{-1}$ is approximately 200 $ZZ \to 4l$ events and approximately 48 $ZZ \to 2l2\nu$ events.

The normalized fiducial cross section as a function of leading Z p_T is in Figure 3.16 for the $ZZ \to 4l$ process and in Figure 3.19 for the $ZZ \to 2l2\nu$ proces.

channel	$\sigma^{Article}$ [fb]	$\sigma^{Rivet}[fb]$
$ZZ \to 4l$	20.9	20.5
$ZZ^* \to 4l$	26.4	25.8
$ZZ \to 2l2\nu$	12.5	12.3

Table 3.3: Comparison of ZZ production cross section results from the paper [32] and from Rivet for all production processes.
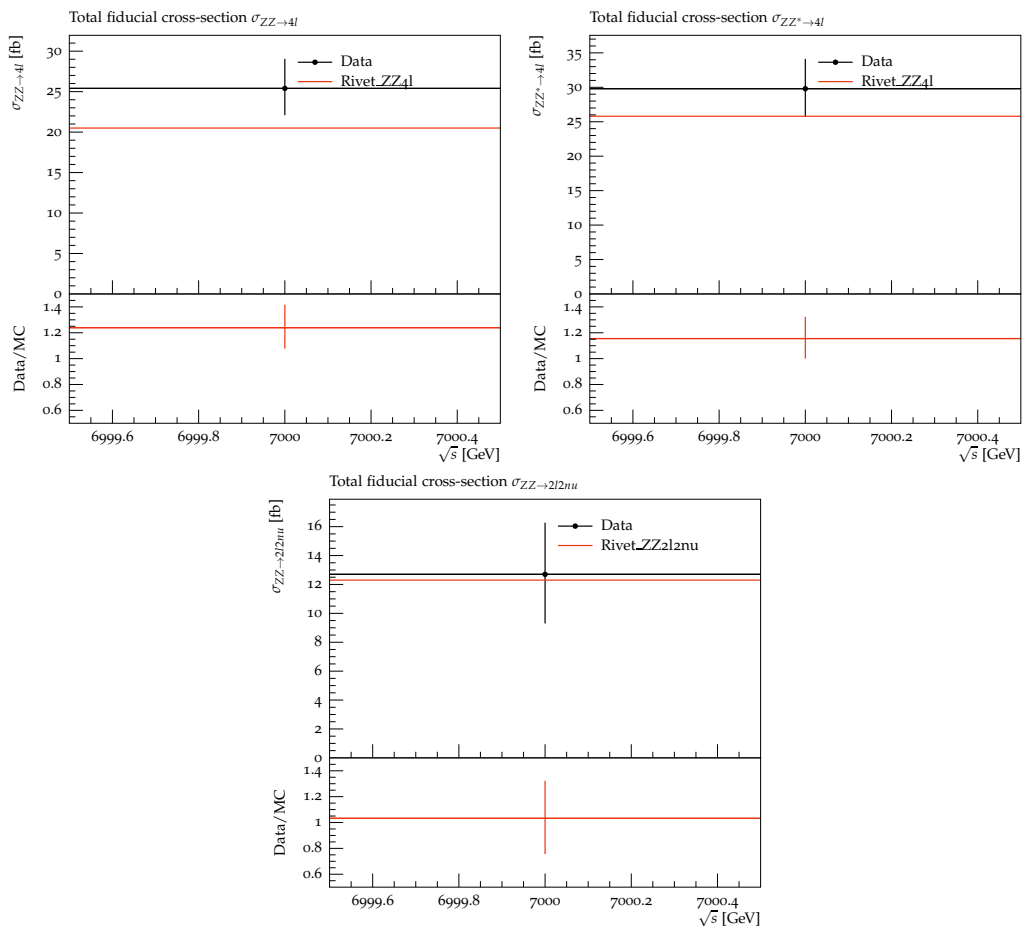

Figure 3.13: Fiducial ZZ production cross section for all production processes plotted with data from HepData [18].
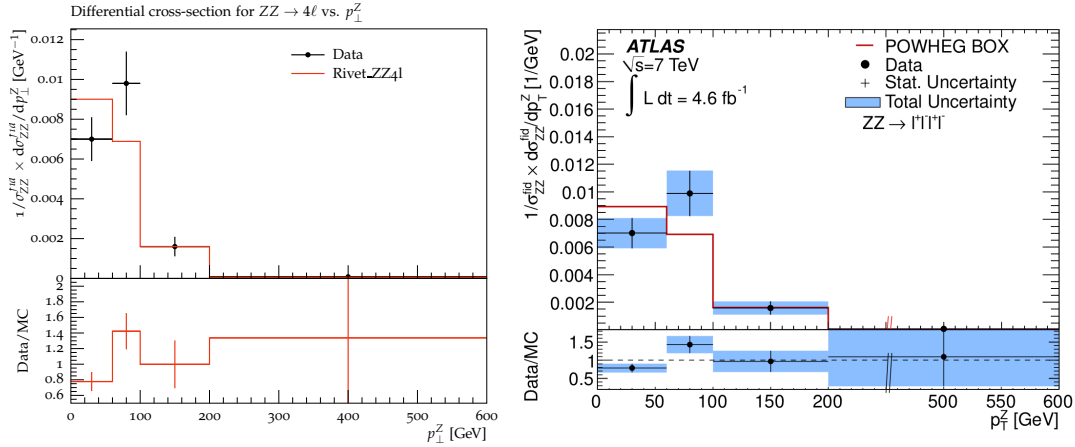
Figure 3.14: The normalized differential fiducial cross section in bins of the leading Z p_T for the ZZ→4l process and Data/MC ratio. Left: The result from Rivet, plotted with data from HepData [18]. Right: The corresponding plot from [32].
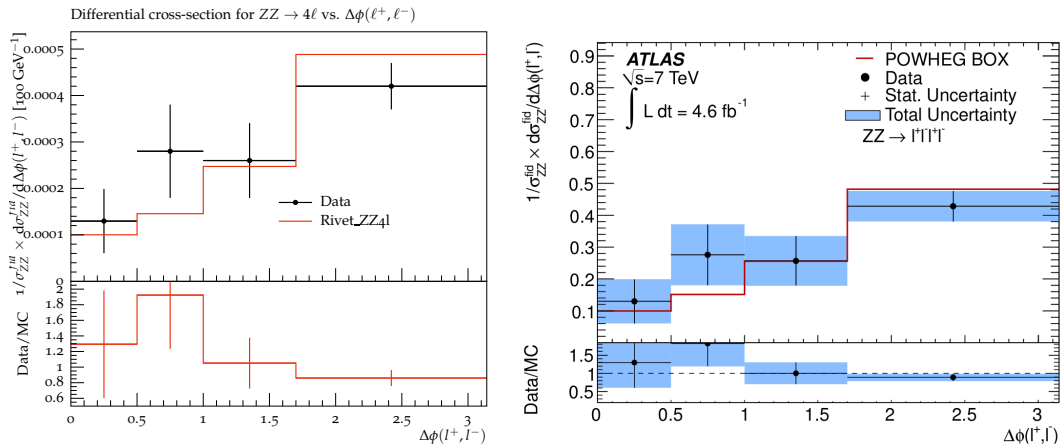

Figure 3.15: The normalized differential fiducial cross section in bins of the angle between the leptons from leading Z boson for the ZZ→4l process and Data/MC ratio. Left: The result from Rivet, plotted with data from HepData [18]. Right: The corresponding plot from [32].
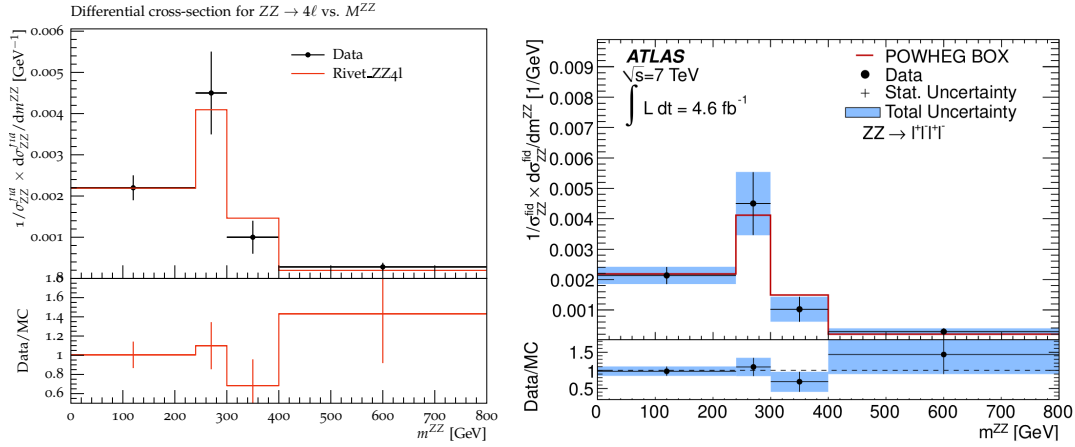
Figure 3.16: The normalized differential fiducial cross section in bins of the ZZ invariant mass for the ZZ→4l process and Data/MC ratio. Left: The result from Rivet, plotted with data from HepData [18]. Right: The corresponding plot from [32].
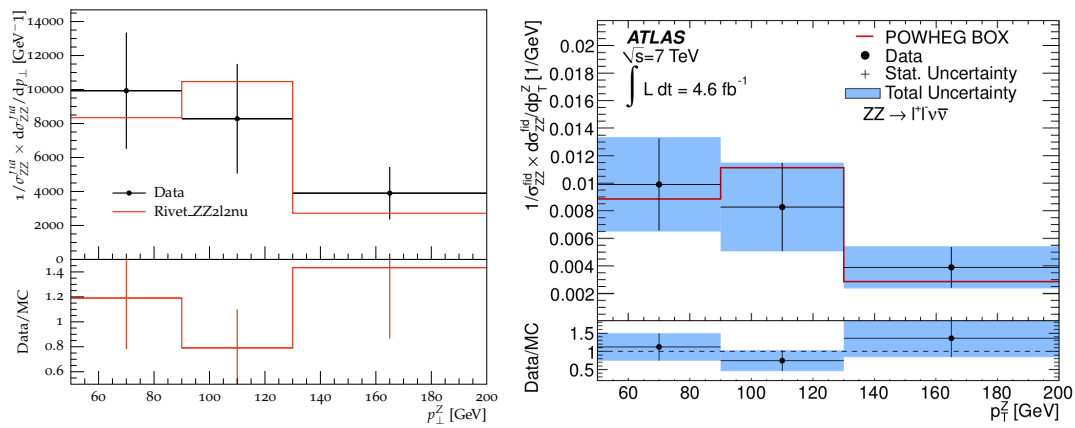

Figure 3.17: The normalized differential fiducial cross section in bins of the leading Z p_T for the ZZ→2l2ν process and Data/MC ratio. Left: The result from Rivet, plotted with data from HepData [18]. Right: The plot from [32].
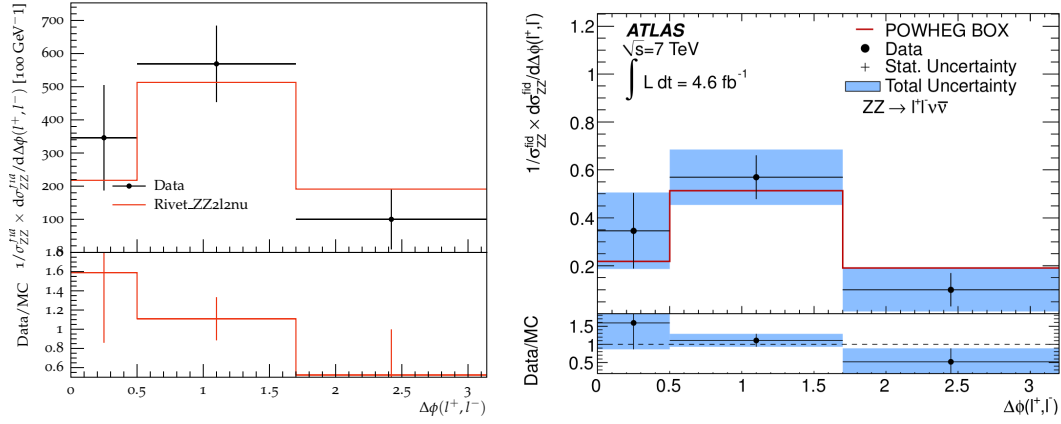
Figure 3.18: The normalized differential fiducial cross section in bins of the angle between the leptons from leading Z boson for the ZZ→2l2ν process and Data/MC ratio. Left: The result from Rivet, plotted with data from HepData [18]. Right: The plot from [32].

Figure 3.19: The normalized differential fiducial cross section in bins of the ZZ transverse mass for the ZZ→2l2ν process and Data/MC ratio. Left: The result from Rivet, plotted with data from HepData [18]. Right: The plot from [32].
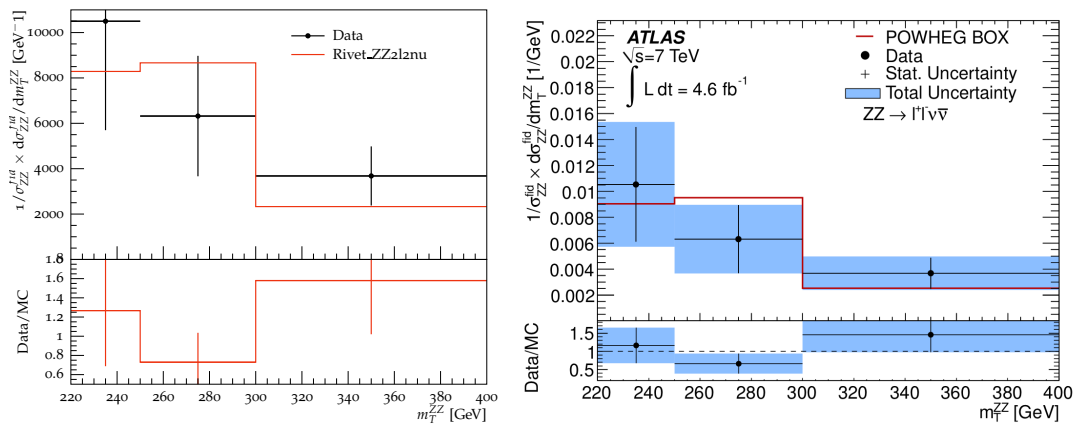
Summary

This thesis discusses diboson production measured in the ATLAS detector at LHC at CERN with a particular emphasis on WW and ZZ production measurements in leptonic decay channels at 7 TeV with integrated luminosity of 4.6 fb^{-1}, which were published in [29] and [32], respectively.

This work was my first experience to get familiar with diboson physics and with its analysis. As a first step, I learned how to calculate the production cross section, using available tools. In this thesis, my reproduction of WW selection at particle level on official ATLAS MC samples in the ROOT framework is presented. The resulted WW production fiducial cross section is in good agreement with the published results in all production channels and also in normalized differential distribution against leading lepton transverse momentum.

As a second step, I learned to work with the Rivet framework. During this part of work, I generated my first MC data in Herwig++. I have successfully implemented both WW and ZZ measurements in Rivet. The implementation is described in this thesis and was presented in detail at WW analysis group and EW group meetings [39, 40]. Both analyses were signed-off by ATLAS Rivet expert. They are included in the new Rivet release (Rivet 2.1.2).

Currently, I am using the Rivet WW analysis to make a dedicated study, in order to figure out the impact of extended ATLAS tracking (and triggering) acceptance on the WW analysis. This extension is considered as one of the ATLAS upgrades. The preliminary results of this study were presented at the corresponding SM Large ETA Taskforce meetings [41, 42].

Bibliography

[1] David Griffiths, Introduction to Elementary Particles, Wiley-VCH, 2008.

[2] Wikimedia Commons standard model, `http://en.wikipedia.org/wiki/File:Standard_Model_of_Elementary_Particles.svg`, Accessed: 2013-11-20.

[3] Robert Craig Group, Measurement of the inclusive jet cross section using the midpoint algorithm in Run II at CDF, 2006.

[4] B. Blossier, Ph. Boucaud, M. Brinet, F. De Soto, X. Du, et al. The Strong running coupling at τ and Z_0 mass scales from lattice QCD, Phys.Rev.Lett., 108:262002, 2012.

[5] J. Beringer et al. (Particle Data Group), 2012.

[6] German F.R. Sborlini, Daniel de Florian, and German Rodrigo, Double collinear splitting amplitudes at next-to-leading order, JHEP, 1401:018, 2014.

[7] Oliver Sim Bruening, Paul Collier, P Lebrun, Stephen Myers, Ranko Ostojic, John Poole, and Paul Proudlock, LHC Design Report, CERN, Geneva, 2004.

[8] ATLAS experiment luminosity public results, `https://twiki.cern.ch/twiki/bin/view/AtlasPublic/LuminosityPublicResults`, Accessed: 2014-12-04.

[9] John M. Campbell, J.W. Huston, and W.J. Stirling, Hard interactions of quarks and gluons: A primer for lhc physics, Rept.Prog.Phys., 70:89, 2007.

[10] W. J. Stirling R. K. Ellis and B. R. Webber, QCD and collider physics, Cambridge University Press, 1996.

[11] Andy Buckley, Jonathan Butterworth, Stefan Gieseke, David Grellscheid, Stefan Hoche, et al, General-purpose event generators for lhc physics, Phys.Rept., 504:145–233, 2011.

[12] G. Corcella, I.G. Knowles, G. Marchesini, S. Moretti, K. Odagiri, et al. HERWIG 6: An Event generator for hadron emission reactions with interfering gluons (including supersymmetric processes), JHEP, 0101:010, 2001.

[13] Torbjorn Sjostrand, Stephen Mrenna, and Peter Z. Skands, PYTHIA 6.4 Physics and Manual, JHEP, 0605:026, 2006.

[14] T. Gleisberg, Stefan. Hoeche, F. Krauss, M. Schonherr, S. Schumann, et al. Event generation with SHERPA 1.1, JHEP, 0902:007, 2009.

[15] John M. Campbell and R.K. Ellis, MCFM for the Tevatron and the LHC, Nucl.Phys.Proc.Suppl., 205-206:10–15, 2010.

[16] Tom Melia, Paolo Nason, Raoul Rontsch, Giulia Zanderighi W+W-, WZ and ZZ production in the POWHEG BOX, JHEP, 1111:078, 2011.

[17] Stefano Frixione and Bryan R. Webber, Matching NLO QCD computations and parton shower simulations, JHEP, 0206:029, 2002.

[18] Andy Buckley and Mike Whalley, HepData reloaded: Reinventing the HEP data archive, PoS, ACAT2010:067, 2010.

[19] HepData database webpage, `http://hepdata.cedar.ac.uk/`, Accessed: 2013-30-12.

[20] Andy Buckley, Tools for event generator tuning and validation, pages 768–773, 2008.

[21] HepMC webpage, `http://lcgapp.cern.ch/project/simu/HepMC/`, Accessed: 2013-13-05.

[22] ATLAS detector and physics performance: Technical Design Report, Technical Design Report ATLAS, CERN, Geneva, 1999, Electronic version not available.

[23] ATLAS experiment electron reconstruction efficiency public results, `https://atlas.web.cern.ch/Atlas/GROUPS/PHYSICS/EGAMMA/PublicPlots/20130926/ATL-COM-PHYS-2013-1287/index.html`, Accessed: 2013-30-12.

[24] Particle physics image bank atlas detector, `http://www.interactions.org/cms/?pid=2100&image_no=CE0155`, Accessed: 2013-30-12.

[25] Georges Aad et al, Measurements of Higgs boson production and couplings in diboson final states with the ATLAS detector at the LHC, Phys.Lett., B726:88–119, 2013.

[26] Standard Model public results summary plots, `https://atlas.web.cern.ch/Atlas/GROUPS/PHYSICS/CombinedSummaryPlots/SM/ATLAS_a_SMSummary_TotalXsect/ATLAS_a_SMSummary_TotalXsect.png`, Accessed: 2014-01-03.

[27] T. Binoth, M. Ciccolini, N. Kauer, and M. Kramer, Gluon-induced W-boson pair production at the LHC, JHEP, 0612:046, 2006.

[28] Karl Jakobs, Physics at the LHC – From Standard Model measurements to Searches for New Physics, 2012.

[29] Georges Aad et al, Measurement of the WW cross section in $\sqrt{s} = 7$ TeV pp collisions with the ATLAS detector and limits on anomalous gauge couplings, Phys.Lett., B712, 2012.

[30] Dieter Zeppenfeld, Low-energy constraints and anomalous triple gauge boson couplings, 1993.

[31] R. Bruneliere et al S. Schael, R. Barate, Improved measurement of the triple gauge-boson couplings Îłww and {ZWW} in collisions, Physics Letters B, 614, 2005.

[32] Georges Aad et al, Measurement of ZZ production in pp collisions at $\sqrt{s} = 7$ TeV and limits on anomalous ZZZ and $ZZ\gamma$ couplings with the ATLAS detector, JHEP, 1303:128, 2013.

[33] Root official web pages, `http://root.cern.ch`, Accessed: 2013-11-20.

[34] MCPlots official web pages, `http://mcplots.cern.ch`, Accessed: 2013-11-25.

[35] Michelangelo L. Mangano, Mauro Moretti, Fulvio Piccinini, Roberto Pittau, and Antonio D. Polosa, ALPGEN, a generator for hard multiparton processes in hadronic collisions, JHEP, 0307:001, 2003.

[36] T Dai, J Ebke, J Elmsheuser, J Gao, D Hall, C Hays, R Kehoe, O Kepka, S Li, J Liu, L Liu, Y Liu, E Monnier, H Peng, M-A Pleier, M Schott, Y Wu, H Yang, Z Zhao, B Zhou, J Zhu, and Y Zhu, Measurement of the WW Production Cross Section in Proton-Proton Collisions at sqrt(s) = 7 TeV with the ATLAS Detector, Technical Report ATL-COM-PHYS-2012-145, CERN, Geneva, Feb 2012, CONF note draft: ATLAS-COM-CONF-2012-024, https://cdsweb.cern.ch/record/1425084.

[37] Matteo Cacciari, Gavin P. Salam, and Gregory Soyez, FastJet User Manual, Eur.Phys.J., C72:1896, 2012.

[38] Simone Alioli, Paolo Nason, Carlo Oleari, and Emanuele Re, A general framework for implementing NLO calculations in shower Monte Carlo programs: the POWHEG BOX, JHEP, 1006:043, 2010.

[39] WW analysis group meeting, `https://indico.cern.ch/event/310818/`, Accessed: 2014-03-05.

[40] SM Electroweak group meeting, `https://indico.cern.ch/event/310681/`, Accessed: 2014-03-05.

[41] 2nd SM Large ETA Taskforce group meeting, `https://indico.cern.ch/event/316315/`, Accessed: 2014-03-05.

[42] 3rd SM Large ETA Taskforce group meeting, `https://indico.cern.ch/event/326930/`, Accessed: 2014-20-06.